

Dynamical system analysis and observational constraints of cosmological models in mimetic gravity

Alberto Fritis,^{1,*} Daniel Villalobos-Silva,^{1,†} Yerko Vásquez,^{1,‡}
 Carlos H. López-Caraballo,^{2,3,§} and Juan Carlos Helo^{1,4,¶}

¹*Departamento de Física, Facultad de Ciencias, Universidad de La Serena,
 Avenida Cisternas 1200, La Serena, Chile.*

²*Instituto de Astrofísica de Canarias, E-38200 La Laguna, Tenerife, Spain.*

³*Departamento de Astrofísica, Universidad de La Laguna, E-38206 La Laguna, Tenerife, Spain.*

⁴*Millennium Institute for Subatomic Physics at the High Energy Frontier (SAPHIR), Fernández Concha 700, Santiago, Chile.*
 (Dated: September 18, 2024)

We study the dynamics of homogeneous and isotropic Friedmann-Lemaître-Robertson-Walker cosmological models with positive spatial curvature within the context of mimetic gravity theory by employing dynamical system techniques. Our analysis yields phase-space trajectories that describe physically relevant solutions, capturing various stages of cosmic evolution. We also employ Bayesian statistical analysis to constrain the cosmological parameters of the models, utilizing data from Type Ia supernovae and Hubble parameter data sets. The observational data sets provide support for the viability of mimetic gravity models, which can effectively describe the late-time accelerated expansion of the universe.

I. INTRODUCTION

Observational data from various surveys and experiments, such as Type Ia Supernovae (SNIa) [1, 2], the cosmic microwave background (CMB) [3, 4], and measurements of the Hubble parameter and baryonic acoustic oscillations (BAO) [5], among others, indicate that the universe is currently undergoing accelerated expansion. This suggests a scenario in which the matter-energy content of the universe comprises two extra components that only interact gravitationally, and their nature remains unknown. One component, referred to as dark energy, plays a crucial role in driving late-time cosmological acceleration. The other component, known as dark matter, behaves as a pressureless fluid and is essential for explaining observed galactic rotation curves.

Gravity theories based on modifications to General Relativity (GR) provide mechanics to explain late-time cosmological acceleration in a more interesting form than introducing an exotic component of matter. Various proposals for modified gravity have been explored in the literature, including $f(R)$ -gravity, where the action of GR is generalized to an arbitrary function of the curvature scalar. For a comprehensive review, see [6]. Gravity models arising from the inclusion of additional curvature invariants in the Lagrangian also have intriguing cosmological implications. Dark energy, for instance, could be elucidated in terms relevant at late time. Moreover, during the early stages of the universe, higher curvature corrections to GR, such as the Starobinsky model of gravity [7], which posits the form $f(R) = R + \alpha R^2$, should be important for the early time inflation. Therefore, modified gravity serves as a natural scenario for a theory that unifies and explains both the inflationary paradigm and the dark energy problem [8]. Ref. [9] reviewed various modified gravities as gravitational alternatives for explaining dark energy. A particularly interesting modification of the gravitational theory is mimetic gravity [10] that has drawn considerable attention to providing a geometric description of dark matter. Theories of this type were introduced previously in [11], which can be obtained through conformal degenerate transformations of the metric [12]. In this theory, the conformal degree of freedom of the gravitational field is isolated by parametrizing the physical metric in terms of an auxiliary metric and a scalar field. This conformal degree of freedom, being dynamical, can serve as a source of cold dark matter. For a comprehensive review of mimetic gravity, see Ref. [13]. In Ref. [14] a potential for the mimetic field was introduced into the action and demonstrated that the model can support both late-time accelerating and inflationary solutions. Several extensions of mimetic gravity have been considered by incorporating higher-order

*Electronic address: albertofripu@gmail.com

†Electronic address: daniel.villalobos@userena.cl

‡Electronic address: yvasquez@userena.cl

§Electronic address: clopez@iac.es

¶Electronic address: jchelo@userena.cl

curvature invariants into the action, [see 15–20], to address the cosmological inflation, or to provide explanations for dark energy. Some models also have the ability to unify and address both the inflationary paradigm and dark energy. Also, Hořava-like and mimetic Horndeski gravity were considered by [21–23]. Yet other theories featuring a scalar degree of freedom include quintessence [24], scalar-tensor theories [25] and Horndeski’s theory [26], among others.

The cosmological equations may be analyzed using nonlinear dynamics techniques. The use of dynamical systems techniques in cosmology is a powerful tool for studying the overall dynamics of a given cosmological model, if the suitable dynamical variables are identified, and thus provide a very good path to qualitative understanding. The phase space and stability test allows us to circumvent the nonlinearities of the cosmological equations and obtain a description of the global dynamics independently of the initial conditions of the universe. This connects critical points to epochs of evolutionary history that are of special relevance. Typically, a late expansion period corresponds to an attractor, while epochs dominated by radiation and matter often correspond to saddle points. Previous studies have applied dynamical system techniques to the analysis of cosmological models, including those involving $f(R)$ -gravity [7, 27, 28], canonical and phantom scalar fields [29–31], and models featuring a mimetic field [32–34] (see also [35–37] and references therein). The dynamical system perspective has also been applied to the study of cosmological models with positive spatial curvature [38, 39]. For a comprehensive exploration of dynamical systems in cosmology, with particular emphasis on the late-time behavior of the universe, please refer to the following references [40, 41].

In this paper we perform a dynamical system analysis of the field equations of mimetic gravity by incorporating a potential for the mimetic field, and also study the observational constraints for models which consider exponential scalar field potentials and inverse quartic potentials. In Ref. [33] a dynamical system study of cosmological models in mimetic gravity was performed considering the flat Friedmann-Lemaître-Robertson-Walker (FLRW) metric. Although recent observations generally support the spatially flat Λ CDM model, notable tensions suggest potential deviations from flatness, sometimes on the order of a few percent [42–44]. Analyses of the Planck 2018 results, as well as the lensing amplitude in the CMB power spectra, reveal an observed enhancement in the lensing amplitude compared to the predictions of the standard Λ CDM model. This discrepancy might be explained by a closed universe, which could provide a physical rationale for the observed effect and indicate a preference for a closed universe with more than 99% confidence. This anomaly might be attributed to new physics, an unresolved systematic error, or merely a statistical fluctuation [42]. Our investigation into dynamical systems is conducted within a cosmological framework described by the FLRW metric, incorporating positive spatial curvature as motivated by these results. We derive phase space trajectories that depict physically relevant solutions representing distinct stages of cosmic evolution. Additionally, we employ a Bayesian statistical analysis to constrain the free parameters of the models, utilizing observational data from the cosmic chronometers (the Hubble database) and the Pantheon database from Type Ia Supernovae.

The paper is structured as follows. In section II we review mimetic gravity theory and write the field equations for the FLRW metric. In section III we write the motion equations as an autonomous dynamical system, identify critical points, and investigate the stability of each point for a generic mimetic field potential. Specific potentials for the mimetic field are explored in detail, and the phase space of each model is analyzed. In section IV we numerically solve the field equations for two mimetic field potentials and compare the results with the non-flat Λ CDM solutions. Then, in section V we constrain the free parameters of the models using Hubble parameter and SNIa measurements, and in section VI we present our conclusions.

II. MIMETIC GRAVITY

In this section, we provide a concise overview of the mimetic gravity theory [10] and write the field equations for the FLRW metric. In mimetic gravity the conformal degree of freedom of the gravitational field is isolated by parametrizing the physical metric $g_{\mu\nu}$ in terms of an auxiliary metric $\hat{g}_{\mu\nu}$ and a scalar field ϕ , referred to as the mimetic field:

$$g_{\mu\nu} = -\hat{g}_{\mu\nu}\hat{g}^{\alpha\beta}\partial_\alpha\phi\partial_\beta\phi. \quad (1)$$

The gravitational action can be varied with respect to the auxiliary metric and the scalar field, rather than the physical metric, and the following constraint is obtained as a consistency condition:

$$g^{\mu\nu}(\hat{g}_{\mu\nu}, \phi)\partial_\mu\phi\partial_\nu\phi + 1 = 0. \quad (2)$$

The field equations obtained from varying the action written in terms of the physical metric and the imposition of the mimetic constraint are completely equivalent to the field equations derived from the action written in terms of the

auxiliary metric. Therefore, the constraint can be implemented at the level of the action by introducing a Lagrange multiplier, λ . Thus, the action describing mimetic gravity can be expressed as:

$$S = \int d^4x \sqrt{-g} \left(\frac{R}{2\kappa^2} - \frac{\lambda}{2} (\partial_\mu \phi \partial^\mu \phi + 1) - V(\phi) \right) + S_m, \quad (3)$$

where $\kappa^2 = 8\pi G$ is the gravitational constant, ϕ is the mimetic field, λ is a Lagrange multiplier field, $V(\phi)$ is a potential for the mimetic field and S_m is a generic matter action that we shall consider as a perfect fluid. The inclusion of a potential for the mimetic field was first considered in Ref. [14].

The variation of the action with respect to the physical metric yields:

$$R_{\mu\nu} - \frac{1}{2} g_{\mu\nu} R = \kappa^2 (T_{\mu\nu} + \lambda \partial_\mu \phi \partial_\nu \phi - g_{\mu\nu} V(\phi)), \quad (4)$$

where $T^{\mu\nu}$ is the energy-momentum tensor of the matter fields. The variation of the action with respect to the Lagrangian multiplier yields the constraint

$$g^{\mu\nu} \partial_\mu \phi \partial_\nu \phi = -1, \quad (5)$$

and the variation with respect to the mimetic field produces

$$\nabla^\mu (\lambda \partial_\mu \phi) - \frac{dV}{d\phi} = 0. \quad (6)$$

We shall consider a cosmological setting where the spacetime is described by the FLRW metric

$$ds^2 = -dt^2 + a(t)^2 \left(\frac{dr^2}{1 - kr^2} + r^2 d\theta^2 + r^2 \sin^2 \theta d\phi^2 \right), \quad (7)$$

where $k = 1, 0, -1$ for a closed, flat and an open universe, respectively.

From the gravitational equations, considering an energy-momentum tensor of a perfect fluid given by $T^\mu_\nu = \text{diag}(-\rho, p, p, p)$ in the co-moving system, the following Friedmann equations are obtained:

$$3H^2 = \kappa^2 (\rho + \lambda + V) - \frac{3k}{a^2}, \quad (8)$$

$$3H^2 + 2\dot{H} = -\kappa^2 (p - V) - \frac{k}{a^2}, \quad (9)$$

where $H = \frac{\dot{a}}{a}$ is the Hubble parameter, and the equation for the mimetic field (6) reads:

$$\dot{\lambda} + 3H\lambda + \frac{dV}{d\phi} = 0. \quad (10)$$

Note that λ represents a non-relativistic dark matter component. Also, using the above equation, together with the Friedmann equations, the conservation equation for the matter content is obtained

$$\dot{\rho} + 3H(\rho + p) = 0. \quad (11)$$

The constraint equation (5) is straightforward to solve and leads to the solution $\phi(t) = t$.

In what follows, we assume a barotropic equation of state for the perfect fluid, i.e., $p = \omega\rho$, where the equation of state parameter is $\omega = 0$ for dust matter and $\omega = 1/3$ for radiation.

It is useful to introduce dimensionless density parameters, which constitute the physical observables, defined by:

$$\Omega_\rho = \frac{\kappa^2 \rho}{3H^2}, \quad \Omega_\lambda = \frac{\kappa^2 \lambda}{3H^2}, \quad \Omega_\phi = \frac{\kappa^2 V}{3H^2}, \quad \Omega_k = -\frac{k}{H^2 a^2}. \quad (12)$$

In terms of these parameters, the Friedmann equation (8) reads:

$$\Omega_\rho + \Omega_\lambda + \Omega_\phi + \Omega_k = 1. \quad (13)$$

It is also useful to introduce the deceleration parameter, defined as $q = -a(t)\ddot{a}(t)/\dot{a}(t)^2$, which quantifies how the expansion rate of the universe changes over time. A value $q < 0$ ($q > 0$) indicates that the expansion of the universe is accelerating (decelerating). The deceleration parameter is related to the density parameters by $q = \frac{1}{2} + \frac{3}{2}\omega\Omega_\rho - \frac{3}{2}\Omega_\phi - \frac{1}{2}\Omega_k$, which will be very useful later. All the parameters defined above constitute the physical observables we are interested in. In the next section we will study the cosmological equations as an autonomous dynamical system.

III. DYNAMICAL SYSTEM APPROACH

In this section we analyze the behavior of the cosmological models with positive spatial curvature $k = 1$ described in the previous section from a dynamical system perspective. To perform the analysis it is convenient to define the following dimensionless dynamical variables:

$$Q = \frac{H}{D}, \quad \tilde{\Omega}_\rho = \frac{\kappa^2 \rho}{3D^2}, \quad \tilde{\Omega}_\lambda = \frac{\kappa^2 \lambda}{3D^2}, \quad \beta = \frac{\kappa \sqrt{V}}{\sqrt{3}D}, \quad \Gamma = -\frac{k}{a^2 D^2}, \quad \zeta = -\frac{1}{\kappa V^{3/2}} \frac{dV}{d\phi}, \quad (14)$$

where $D \equiv \sqrt{H^2 + \frac{k}{a^2}}$. Here Q is a compact variable that can take values only in the interval $[-1, 1]$, where $Q > 0$ corresponds to an expanding epoch, and $Q < 0$ corresponds to a contracting epoch.

The Friedmann equation (8) and the definition of D yield the constraints:

$$\tilde{\Omega}_\rho + \tilde{\Omega}_\lambda + \beta^2 = 1, \quad (15)$$

$$Q^2 - \Gamma = 1. \quad (16)$$

Next, using these constraints and introducing the new time variable $d\tau = Ddt$, the cosmological equations can be written as an autonomous dynamical system:

$$Q' = (1 - Q^2) \left(\frac{3}{2} \left((1 + \omega)(\beta^2 - 1) + \omega \tilde{\Omega}_\lambda \right) + 1 \right), \quad (17)$$

$$\tilde{\Omega}'_\lambda = -3Q\tilde{\Omega}_\lambda + \sqrt{3}\beta^3\zeta - 3Q\tilde{\Omega}_\lambda \left((1 + \omega)(\beta^2 - 1) + \omega \tilde{\Omega}_\lambda \right), \quad (18)$$

$$\beta' = -\frac{\sqrt{3}}{2}\beta^2\zeta - \frac{3}{2}\beta Q \left((1 + \omega)(\beta^2 - 1) + \omega \tilde{\Omega}_\lambda \right), \quad (19)$$

$$\zeta' = -\sqrt{3}\zeta^2\beta \left(\mu(\zeta) - \frac{3}{2} \right), \quad (20)$$

where we have defined $\mu = \ddot{V}V/\dot{V}^2$ and the prime denotes a derivative with respect to τ . The dimensionless dynamical variables constitute the basis of the phase space, and the first order differential equations (17)-(20) are completely equivalent to the original field equations and give the phase trajectories. Additionally, the weak energy condition $\tilde{\Omega}_\rho \geq 0$, in conjunction with Eq. (15), produces $-\infty < \tilde{\Omega}_\lambda \leq 1 - \beta^2$. Therefore, the physical phase space is contained in the region $\beta > 0$, $\zeta \in \mathbb{R}$, $Q \in [-1, 1]$ and $-\infty < \tilde{\Omega}_\lambda \leq 1 - \beta^2$.

Furthermore, it can be found that $\tilde{\Omega}'_\rho = -3Q\tilde{\Omega}_\rho \left((1 + \omega)\beta^2 + \omega \tilde{\Omega}_\lambda \right)$, which shows that $\tilde{\Omega}_\rho = 0$ is an invariant submanifold. The invariant submanifolds of the reduced dynamical system are the following:

- $\tilde{\Omega}_\rho = 0$, which corresponds to the $\rho = 0$ boundary.
- $Q = \pm 1$ are the flat submanifolds ($k = 0$).
- The $\beta = 0$ submanifold.
- The $\zeta = 0$ submanifold, with $\zeta^2\mu(\zeta) = 0$ for $\zeta = 0$.

The dynamical variables defined to describe the physical system are not physical observables but are related to the density parameters by $\Omega_\rho = \frac{\tilde{\Omega}_\rho}{Q^2}$, $\Omega_\lambda = \frac{\tilde{\Omega}_\lambda}{Q^2}$, $\Omega_\phi = \frac{\beta^2}{Q^2}$, $\Omega_k = 1 - \frac{1}{Q^2}$.

A. Critical Points

Applying the standard procedure of cosmological dynamical systems, we start by looking at the critical points of the system (17)–(20) for an arbitrary scalar field potential.

The critical points correspond to the points where the system is in equilibrium and are defined by the vanishing of the right-hand sides of Eqs. (17)–(20). In Table I we show the critical points of the system and the values of some physical quantities associated with each of them. Note that, with the exception of points A_1 , A_2 and D , all other points lie on the flat submanifolds.

We now examine the linear stability of the critical points by linearizing the evolution equations in the vicinity of these critical points. The Jacobian matrix of the system is given by:

$$\begin{bmatrix} -2Q \left(\frac{3}{2} ((\beta^2 - 1)(\omega + 1) + \bar{\Omega}_\lambda \omega) + 1 \right) & \frac{3}{2} \omega (1 - Q^2) & 3\beta(1 - Q^2)(1 + \omega) & 0 \\ -3\bar{\Omega}_\lambda (\beta^2(1 + \omega) + \omega(\bar{\Omega}_\lambda - 1)) & -3Q(\beta^2(1 + \omega) + \omega(2\bar{\Omega}_\lambda - 1)) & 3\beta(\sqrt{3}\zeta\beta - 2Q\bar{\Omega}_\lambda(\omega + 1)) & \sqrt{3}\beta^3 \\ -\frac{3}{2}\beta((\beta^2 - 1)(\omega + 1) + \omega\bar{\Omega}_\lambda) & -\frac{3}{2}Q\beta\bar{\Omega}_\lambda & -\sqrt{3}\beta\zeta + \frac{3Q}{2}((1 - 3\beta^2)(1 + \omega) - \omega\bar{\Omega}_\lambda) & -\frac{\sqrt{3}}{2}\beta^2 \\ 0 & 0 & -\sqrt{3}\zeta^2(\mu(\zeta) - \frac{3}{2}) & -\sqrt{3}\zeta\beta\left(\zeta\frac{d\mu(\zeta)}{d\zeta} + 2\mu(\zeta) - 3\right) \end{bmatrix}$$

The eigenvalues of the Jacobian matrix, computed at a critical point, enable the analysis of the linear stability of that point. In Table II we present the eigenvalues corresponding to each critical point. However, linear stability theory can only be applied to examine the stability of points whose eigenvalues have a non-null real part (referred to as hyperbolic critical points). To assess the stability of non-hyperbolic critical points it is necessary to employ methods beyond linear stability theory, such as the Lyapunov method or centre manifold theory. By employing the centre manifold, we shall analyze certain cases that cannot be categorized as hyperbolically stable or unstable because of the presence of null eigenvalues in the variation matrix. The cases that always satisfy this condition are analyzed, as well as those that could meet this condition in specific circumstances.

TABLE I: Fixed points of the dynamical system (17)–(20) and some physical quantities for an arbitrary mimetic field potential. ζ_* is the solution of $\mu(\zeta) - 3/2 = 0$

Label	$\bar{\Omega}_\lambda$	β	ζ	Q	Existence	Ω_ρ	Ω_λ	Ω_ϕ	Ω_k	q
A_1	$-\frac{2}{3\omega} + (1 - \beta^2)(1 + \frac{1}{\omega})$	$\beta \geq \frac{1}{\sqrt{3}}$	0	0	$\omega \neq 0, \zeta^2\mu = 0$ for $\zeta = 0$	∞	∞ for $\bar{\Omega}_\lambda > 0$, $-\infty$ for $\bar{\Omega}_\lambda < 0$	∞	$-\infty$	∞
A_2	$\bar{\Omega}_\lambda \leq \frac{2}{3}$	$\frac{1}{\sqrt{3}}$	0	0	$\omega = 0, \zeta^2\mu = 0$ for $\zeta = 0$	∞	∞ for $\bar{\Omega}_\lambda > 0$, $-\infty$ for $\bar{\Omega}_\lambda < 0$	∞	$-\infty$	∞
B_+	0	1	0	1	$\zeta^2\mu = 0$ for $\zeta = 0$	0	0	1	0	-1
B_-	0	1	0	-1	$\zeta^2\mu = 0$ for $\zeta = 0$	0	0	1	0	-1
C_{1+}	$-\frac{3(1+\omega)^3}{\omega\zeta_*^2}$	$\frac{(1+\omega)\sqrt{3}}{\zeta_*}$	ζ_*	1	$\omega \neq 0, \zeta_* > 0$	$\frac{3+\omega(\zeta_*^2+6+3\omega)}{\zeta_*^2\omega}$	$-\frac{3(1+\omega)^3}{\omega\zeta_*^2}$	$\frac{3(1+\omega)^2}{\zeta_*^2}$	0	$\frac{1}{2}(1+3\omega)$
C_{1-}	$-\frac{3(1+\omega)^3}{\omega\zeta_*^2}$	$-\frac{(1+\omega)\sqrt{3}}{\zeta_*}$	ζ_*	-1	$\omega \neq 0, \zeta_* < 0$	$\frac{3+\omega(\zeta_*^2+6+3\omega)}{\zeta_*^2\omega}$	$-\frac{3(1+\omega)^3}{\omega\zeta_*^2}$	$\frac{3(1+\omega)^2}{\zeta_*^2}$	0	$\frac{1}{2}(1+3\omega)$
C_{2+}	$\frac{1}{6}\zeta_*(\sqrt{12+\zeta_*^2} - \zeta_*)$	$\frac{\sqrt{12+\zeta_*^2}-\zeta_*}{2\sqrt{3}}$	ζ_*	1		0	$\frac{1}{6}\zeta_*(\sqrt{12+\zeta_*^2} - \zeta_*)$	$\frac{1}{12}(\sqrt{\zeta_*^2+12} - \zeta_*)^2$	0	$\frac{1}{4}\zeta_*(\sqrt{\zeta_*^2+12} - \zeta_*) - 1$
C_{2-}	$-\frac{1}{6}\zeta_*(\sqrt{12+\zeta_*^2} + \zeta_*)$	$\frac{\sqrt{12+\zeta_*^2}+\zeta_*}{2\sqrt{3}}$	ζ_*	-1		0	$-\frac{1}{6}\zeta_*(\sqrt{12+\zeta_*^2} + \zeta_*)$	$\frac{1}{12}(\sqrt{\zeta_*^2+12} + \zeta_*)^2$	0	$-\frac{1}{4}\zeta_*(\sqrt{\zeta_*^2+12} + \zeta_*) - 1$
D	$\frac{2}{3}$	$\frac{1}{\sqrt{3}}$	ζ_*	$\frac{\zeta_*}{2}$	$\zeta_* \neq 0, Q \neq \pm 1$	0	$\frac{8}{3\zeta_*^2}$	$\frac{4}{3\zeta_*^2}$	$1 - \frac{4}{\zeta_*^2}$	0
L_{1+}	0	0	ζ	1	critical line for all ζ for $\omega \neq 0$	1	0	0	0	$\frac{1}{2}(1+3\omega)$
L_{2+}	1	0	ζ	1	critical line for all ζ for $\omega \neq 0$	0	1	0	0	$\frac{1}{2}$
L_{1-}	0	0	ζ	-1	critical line for all ζ for $\omega \neq 0$	1	0	0	0	$\frac{1}{2}(1+3\omega)$
L_{2-}	1	0	ζ	-1	critical line for all ζ for $\omega \neq 0$	0	1	0	0	$\frac{1}{2}$
P_+	$\bar{\Omega}_\lambda \leq 1$	0	ζ	1	critical plane for $\omega = 0$	$1 - \Omega_\lambda$	$\Omega_\lambda \leq 1$	0	0	$\frac{1}{2}$
P_-	$\bar{\Omega}_\lambda \leq 1$	0	ζ	-1	critical plane for $\omega = 0$	$1 - \Omega_\lambda$	$\Omega_\lambda \leq 1$	0	0	$\frac{1}{2}$

The information presented in Tables I and II enables the description of the behavior of the dynamical system in the neighborhood of each critical point. In what follows ζ_* corresponds to the solution of $\mu(\zeta) - 3/2 = 0$.

- A_1 and A_2 correspond to critical curves where Q vanishes and the deceleration parameter diverges, thus resembling the behavior of the Einstein static solution where $H = 0$ and $\dot{H} = 0$. A_1 exists for $\omega \neq 0$ and $\zeta^2\mu = 0$ for $\zeta = 0$, whereas A_2 exists for $\omega = 0$ and $\zeta^2\mu = 0$ for $\zeta = 0$. Moreover, these curves are non-hyperbolic and act as saddles, as the non-zero eigenvalues have opposite signs.
- B_+ exists if $\zeta^2\mu = 0$ for $\zeta = 0$, representing an expanding de Sitter accelerated solution dominated by the mimetic field, $\Omega_\phi = 1$. The stability analysis involves examining the sign of $-\sqrt{3}\frac{d}{d\zeta}(\zeta^2\mu(\zeta))$ at $\zeta = 0$. If it

TABLE II: Eigenvalues and stability of fixed points of the dynamical system (17)-(20). In the formulas below we have defined $\xi_{\pm}(\zeta_*) = \zeta_*^2 \pm \zeta_* \sqrt{\zeta_*^2 + 12} + 12\omega$. ζ_* is the solution of $\mu(\zeta) - 3/2 = 0$

Label	λ_1	λ_2	λ_3	λ_4	Dynamical Character
A_1	$-\frac{\sqrt{-(1+3\omega)+9\beta^2(1+\omega)}}{\sqrt{2}}$	$\frac{\sqrt{-(1+3\omega)+9\beta^2(1+\omega)}}{\sqrt{2}}$	$-\sqrt{3}\beta \frac{d}{d\zeta}(\zeta^2\mu(\zeta)) _{\zeta=0}$	0	non-hyperbolic, behaves as saddle
A_2	-1	1	$-\frac{d}{d\zeta}(\zeta^2\mu(\zeta)) _{\zeta=0}$	0	non-hyperbolic, behaves as saddle
B_+	-2	$-3(1+\omega)$	$-\sqrt{3}\beta \frac{d}{d\zeta}(\zeta^2\mu(\zeta)) _{\zeta=0}$	-3	mostly attractive, potentially non-hyperbolic
B_-	2	$3(1+\omega)$	$-\sqrt{3}\beta \frac{d}{d\zeta}(\zeta^2\mu(\zeta)) _{\zeta=0}$	3	mostly repulsive, potentially non-hyperbolic
C_{1+}	$-\frac{3((1-\omega)\zeta_* + \sqrt{24(1+\omega)^3 + (1+3\omega)^2\zeta_*^2})}{4\zeta_*}$	$-\frac{3((1-\omega)\zeta_* - \sqrt{24(1+\omega)^3 + (1+3\omega)^2\zeta_*^2})}{4\zeta_*}$	$-3(1+\omega)\zeta_*\mu'(\zeta_*)$	$1+3\omega$	saddle
C_{1-}	$\frac{3((1-\omega)\zeta_* + \sqrt{24(1+\omega)^3 + (1+3\omega)^2\zeta_*^2})}{4\zeta_*}$	$\frac{3((1-\omega)\zeta_* - \sqrt{24(1+\omega)^3 + (1+3\omega)^2\zeta_*^2})}{4\zeta_*}$	$3(1+\omega)\zeta_*\mu'(\zeta_*)$	$-(1+3\omega)$	saddle
C_{2+}	$-\frac{3}{8}(\xi_-(\zeta_*) + 8(1-\omega) + \frac{1}{3} \xi_-(\zeta_*))$	$-\frac{3}{8}(\xi_-(\zeta_*) + 8(1-\omega) - \frac{1}{3} \xi_-(\zeta_*))$	$\frac{1}{2}\zeta_*^2(\zeta_* - \sqrt{\zeta_*^2 + 12})\mu'(\zeta_*)$	$-2 + \frac{1}{2}\zeta_*(-\zeta_* + \sqrt{\zeta_*^2 + 12})$	see Appendix A
C_{2-}	$\frac{3}{8}(\xi_+(\zeta_*) + 8(1-\omega) - \frac{1}{3} \xi_+(\zeta_*))$	$\frac{3}{8}(\xi_+(\zeta_*) + 8(1-\omega) + \frac{1}{3} \xi_+(\zeta_*))$	$-\frac{1}{2}\zeta_*^2(\zeta_* + \sqrt{\zeta_*^2 + 12})\mu'(\zeta_*)$	$2 + \frac{1}{2}\zeta_*(\zeta_* + \sqrt{\zeta_*^2 + 12})$	see Appendix A
D	$-1 - \frac{\zeta_*}{2}$	$-\frac{1}{2}\zeta_*(1+3\omega)$	$-\zeta_*^2\mu'(\zeta_*)$	$1 - \frac{\zeta_*}{2}$	see analysis
L_{1+}	3ω	$\frac{3(1+\omega)}{2}$	$1+3\omega$	0	non-hyperbolic, unstable
L_{2+}	1	0	-3ω	$\frac{3}{2}$	saddle
L_{1-}	-3ω	$-\frac{3}{2}(1+\omega)$	$-(1+3\omega)$	0	non-hyperbolic
L_{2-}	-1	0	3ω	$-\frac{3}{2}$	saddle
P_+	0	0	$\frac{3}{2}$	1	non-hyperbolic, unstable
P_-	0	0	$-\frac{3}{2}$	-1	non-hyperbolic

is negative, the critical point is an attractor; if it is positive, it is a saddle point. If $-\sqrt{3}\beta \frac{d}{d\zeta}(\zeta^2\mu(\zeta))|_{\zeta=0}$ equals 0, the point is non-hyperbolic, and its stability is analyzed using the centre manifold method, as detailed in appendix A. In this case, several possibilities arise:

- If $-\sqrt{3}\beta \frac{d^2}{d\zeta^2}(\zeta^2\mu(\zeta))|_{\zeta=0} \neq 0$, the critical point will manifest unstable behavior in a specific direction (it is easy to see that the direction is locally ζ)
- Otherwise, with $\sigma = -\sqrt{3}\beta \frac{d^3}{d\zeta^3}(\zeta^2\mu(\zeta))|_{\zeta=0}$, if $\sigma < 0$ it has an asymptotically stable behavior. If $\sigma > 0$ it displays unstable behavior in this direction. If $\sigma = 0$, higher order terms must be considered in the series.
- B_- is the contracting analogue of B_+ and is unstable. For $-\sqrt{3}\beta \frac{d}{d\zeta}(\zeta^2\mu(\zeta))|_{\zeta=0} = 0$, it is non-hyperbolic, leading to the following possibilities:
 - If $-\sqrt{3}\beta \frac{d^2}{d\zeta^2}(\zeta^2\mu(\zeta))|_{\zeta=0} \neq 0$, the critical point will manifest stable behavior in one direction only (locally ζ)
 - Otherwise, with $\sigma = -\sqrt{3}\beta \frac{d^3}{d\zeta^3}(\zeta^2\mu(\zeta))|_{\zeta=0}$, if $\sigma < 0$, the point shows stable behavior in one direction. If $\sigma > 0$, its behavior is unstable in all directions. If $\sigma = 0$ higher-order terms must be considered in the series.
- C_{1+} and C_{1-} behave as scaling solutions, which can alleviate the cosmic coincidence problem. In these scenarios, both a scalar field and matter densities coexist, meaning that the universe undergoes evolution influenced by both matter (baryonic plus mimetic matter) and the scalar field. However, the universe expands as if it were dominated by matter. Here, the deceleration parameter is given by $q = \frac{1}{2}(1+3\omega) > 0$ for matter and radiation, indicating non-accelerating solutions. The stability analysis reveals that these are saddle points.
- The point C_{2+} stands for an expanding cosmological solution where the mimetic matter and the mimetic field dominate. When $\zeta_* < 2$, accelerating solutions are possible. In the limit as $\zeta_* \rightarrow 0$, the universe is predominantly governed by the mimetic field, resulting in an expanding de Sitter solution. Note that point B_+ is a special case of C_{2+} with $\zeta_* = 0$. Conversely, C_{2-} is the contracting analogue of C_{2+} .
- Critical point D corresponds to a uniformly expanding/contracting solution ($q = 0$) and exists for $\zeta_* \neq 0$ and $Q \neq \pm 1$.
 - If $-2 < \zeta_* < 2$, it behaves as saddle
 - If $\zeta_* = -2$, and for $\mu'(\zeta) > 0$, it behaves as a saddle. We are interested in the case $\mu'(\zeta) < 0$. $\mu'(\zeta) = 0$, however, is a more particular case that we shall rule out. There is also the possibility of choosing this value to coincide with another eigenvalue, and it is possible that the system may not be diagonalizable. If this is the case, the variation matrix must be expressed in its Jordan form to separate the spaces associated with each eigenvalue. We do not intend to analyze these special cases here.

* For $\mu'(\zeta) < 0$ only one direction (locally Q) shows attractive behavior.

Note that for this value of ζ_* , D does not match $Q \neq -1$; however, for this value it matches C_{2-} , which is covered in depth in appendix A

– If $\zeta_* = 2$, and for $\mu'(\zeta) < 0$ it behaves as a saddle. Therefore, we are interested in the case $\mu'(\zeta) > 0$. Besides, there may be exceptions equivalent to the previous case that we shall not analyze.

* For $\mu'(\zeta) > 0$ only one direction (locally Q) shows repulsive behavior.

Note that for this value of ζ_* , D does not match $Q \neq 1$; however, for this value it does match C_{2+} , which is covered in depth in appendix A.

- L_{1+} is a critical line that corresponds to a non-accelerating radiation-dominated universe, it never represents a stable line (note that, as shown in Table I, the matter component is dominant, and in the evaluated cases, only the case with $\omega = 1/3$ is possible.).
- L_{2+} is a critical line that corresponds to a universe dominated by mimetic dark matter, and its behavior is similar to that of L_{1+} .
- L_{1-} and L_{2-} are the contracting analogs of lines L_{1+} and L_{2+} , respectively.
- P_+ is a non-hyperbolic unstable critical plane that describes a non-accelerating universe dominated by baryonic plus mimetic dark matter, and P_- is its contracting analog.

B. Dynamics in invariant manifolds

Given the existence of principal invariant submanifolds and under the good behavior of the system variables in them, it becomes possible to gain some level of understanding of the neighborhoods of the submanifolds by analyzing them. For this reason, the submanifolds $\beta = 0$, $\zeta = 0$ and $\tilde{\Omega}_\rho = 0$ are good indicators. The first two do not depend on the shape of the potential, therefore, their dynamics is independent of the mimetic field potential. In contrast, $\tilde{\Omega}_\rho$ and $Q = \pm 1$ could only be analyzed given the potential. However, the submanifolds $Q = \pm 1$ do not represent their neighborhoods well. Instead, they constitute inaccessible exceptions, and they will not be the subject of further analysis.

1. Submanifold $\zeta = 0$

The critical points and their respective dynamics in the submanifold are detailed in Figs. 1 and 2:

- For $\omega = 0$: A_2 exhibits saddle behavior, P_+ displays repulsive behavior in directions other than the critical axis and P_- is the contracting analogue of P_+ .
- For $\omega = 1/3$: A_1 shows saddle behavior, L_{1+} exhibits repulsive behavior, L_{2+} exhibits saddle behavior, L_{1-} shows attractor behavior and L_{2-} displays saddle behavior.
- For both values of ω : B_+ shows attractor behavior and B_- exhibits repulsive behavior.

In Figs. 1 and 2 we depict the phase portraits of the invariant submanifold $\zeta = 0$ for $\omega = 0$ and $\omega = 1/3$, respectively. The phase space is divided into two halves, one corresponding to a contracting epoch ($Q < 0$) and the other to an expanding epoch ($Q > 0$). For $\omega = 0$ we can see that certain trajectories that are past asymptotic to the matter-dominated critical line P_+ , with a sufficiently small value of Ω_ϕ after some expansion enter the contracting phase space and collapse to a big crunch at P_- . There are also models starting from P_+ with a high enough value of Ω_ϕ that evolve to the future attractor B_+ , which represents an expanding de Sitter accelerated solution dominated by the mimetic field. Some trajectories which are past asymptotic to B_- evolve to point B_+ , while others evolve to P_- . There are also trajectories which are past asymptotic as well as future asymptotic to the Einstein static solution, line A_2 . Similar behavior is found for the case $\omega = 1/3$, with the matter-dominated critical line P_+/P_- replaced by the points L_{1+}/L_{1-} (ordinary matter dominated) and L_{2+}/L_{2-} (mimetic matter dominated) and A_2 by A_1 .

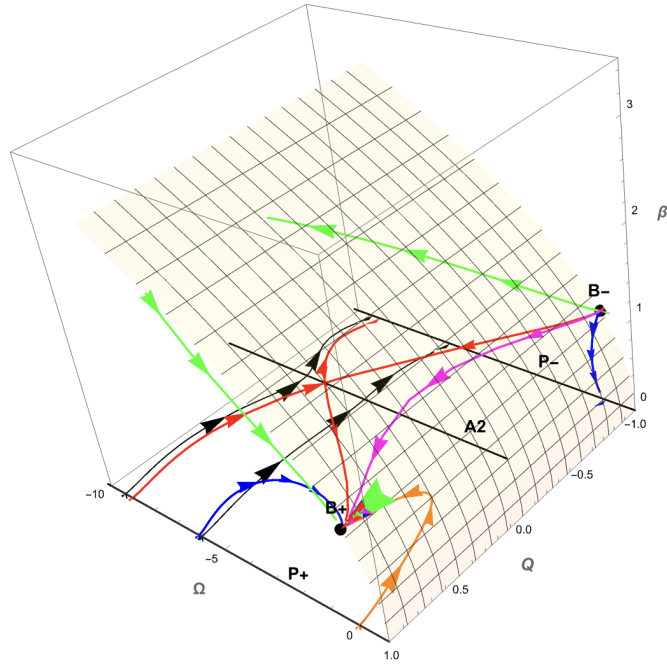


FIG. 1: Phase portrait of the invariant submanifold $\zeta = 0$ for $\omega = 0$, here Ω is the dynamical variable $\tilde{\Omega}_\lambda$. Some trajectories starting from the matter-dominated critical line P_+ as $\tau \rightarrow -\infty$ converge to the dark energy dominated point B_+ as $\tau \rightarrow \infty$, while others after some expansion begin contracting and collapse to a big crunch at P_- . Some trajectories which are past asymptotic to B_- evolve to the future attractor B_+ , while others evolve to P_- .

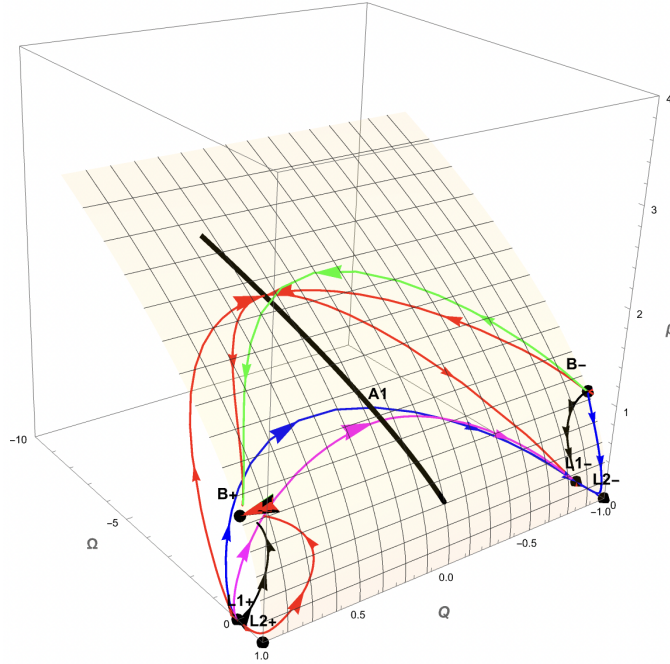


FIG. 2: Phase portrait of the invariant submanifold $\zeta = 0$ for $\omega = 1/3$, here Ω is the dynamical variable $\tilde{\Omega}_\lambda$. Some trajectories starting from the ordinary matter-dominated critical line L_{1+} and from the dark matter dominated critical line L_{2+} as $\tau \rightarrow -\infty$ converge to the dark energy dominated point B_+ as $\tau \rightarrow \infty$, while others after some expansion begin contracting and collapse to a big crunch at P_- . Some trajectories which are past asymptotic to B_- evolve to the future attractor B_+ , while others evolve to L_{1-} or L_{2-} .

The behavior of the variable ζ for some points close to the submanifold depends almost exclusively on the potential. By explicitly analyzing the behavior of ζ as a function of t , one can gain insights into the curves and expect a relationship between the behaviors with cosmological time and transformed time. However, for more precision, it is advisable to examine the dynamics around the points belonging to the submanifold by using either the eigenvalues of the variation matrix, if applicable, or the center manifold, if necessary. Lastly, whether the submanifold is reachable from outside will depend on the potential.

2. Submanifold $\beta = 0$

The critical points and their corresponding dynamics in the submanifold are illustrated in Fig. 3:

- For $\omega = 0$: P_+ exhibits repulsive behavior in the noncritical axes, while P_- displays attractive behavior in the noncritical axes.
- For $\omega = 1/3$: L_{1+} exhibits repulsive behavior, L_{1-} has attractive behavior, and both L_{2+} and L_{2-} behave as saddles.

Note that for $\beta = 0$, the equation for ζ vanishes (assuming that $\zeta^2(\mu(\zeta) - 3/2)$ does not diverge for the conditions in which β vanishes); the contribution of ζ to the remaining system is also null; therefore, it is enough to graph the coordinates $(Q, \tilde{\Omega}_\lambda)$. In Fig. 3 we plot the phase portrait of the invariant submanifold $\beta = 0$ for $\omega = 0$ and $\omega = 1/3$. The trajectories observed are past asymptotic to a matter-dominated critical line which after some expansion enter the contracting phase space and collapse to a big crunch.

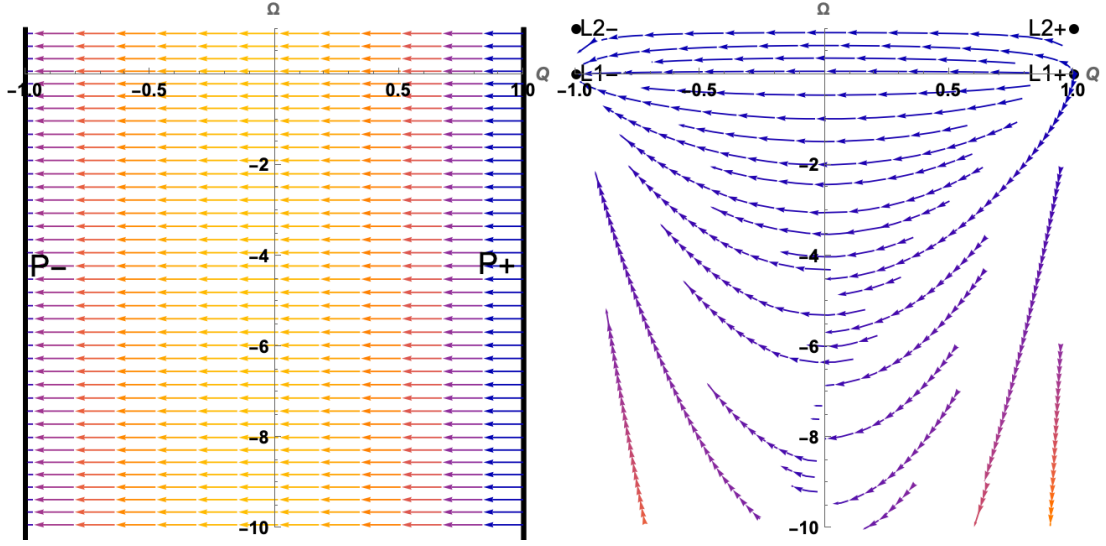


FIG. 3: Phase portraits of the invariant submanifold $\beta = 0$ for $\omega = 0$ (left panel) and $\omega = 1/3$ (right panel), Ω is the dynamical variable $\tilde{\Omega}_\lambda$. Trajectories starting from the matter-dominated line P_+ as $\tau \rightarrow -\infty$ end at P_- as $\tau \rightarrow \infty$. Analogously, trajectories starting from the ordinary matter-dominated line L_{1+} or from the dark matter dominated line L_{2+} end at L_{1-} or L_{2-} .

Analysis of the behavior on the β axis, which is important for determining whether a trajectory stays in the neighborhood of the submanifold, is difficult owing to the dependence of β on V and D . It is possible to obtain this information by analyzing the behavior in the neighborhood of the critical points belonging to the submanifold. For instance, for P_- the behavior is attractive, while for P_+ it is repulsive along this axis. Again, regarding whether the submanifold can be accessed from an external point depends on the potential.

C. Specific potentials

In this section we explore the dynamics of the system for two specific potentials of the mimetic field: the inverse square potential and the exponential potential.

1. Inverse square potential

Here, we consider the potential $V(\phi) = \gamma/\phi^2$, where γ is a coupling constant. In this case we find that $\mu(\zeta) = 3/2$ and $\zeta = \frac{2}{\kappa\gamma^{1/2}}$ become constants; therefore, the dynamical system reduces to a three-dimensional autonomous dynamical system given by Eqs. (17)-(19) with ζ constant.

The critical points of the system are shown in Table III and the eigenvalues of the Jacobian matrix that characterize their dynamical behavior are shown in Table IV. Note that the Einstein static solutions A_1 and A_2 , and also the solutions B_+ and B_- , disappear for this potential.

TABLE III: Fixed points of the dynamical system (17)-(20) and some physical quantities for the inverse square potential. In the formulas below $\zeta = \frac{2}{\kappa\gamma^{1/2}}$.

Label	$\tilde{\Omega}_\lambda$	β	Q	Existence	Ω_ρ	Ω_λ	Ω_ϕ	Ω_k	q
C_{1+}	$-\frac{3(1+\omega)^3}{\omega\zeta^2}$	$\frac{(1+\omega)\sqrt{3}}{\zeta}$	1	$\omega \neq 0, \zeta > 0$	$\frac{3+\omega(\zeta^2+6+3\omega)}{\zeta^2\omega}$	$-\frac{3(1+\omega)^3}{\omega\zeta^2}$	$\frac{3(1+\omega)^2}{\zeta^2}$	0	$\frac{1}{2}(1+3\omega)$
C_{1-}	$-\frac{3(1+\omega)^3}{\omega\zeta^2}$	$-\frac{(1+\omega)\sqrt{3}}{\zeta}$	-1	$\omega \neq 0, \zeta < 0$	$\frac{3+\omega(\zeta^2+6+3\omega)}{\zeta^2\omega}$	$-\frac{3(1+\omega)^3}{\omega\zeta^2}$	$\frac{3(1+\omega)^2}{\zeta^2}$	0	$\frac{1}{2}(1+3\omega)$
C_{2+}	$\frac{1}{6}\zeta(\sqrt{12+\zeta^2}-\zeta)$	$\frac{\sqrt{12+\zeta^2}-\zeta}{2\sqrt{3}}$	1		0	$\frac{1}{6}\zeta(\sqrt{12+\zeta^2}-\zeta)$	$\frac{1}{12}(\sqrt{\zeta^2+12}-\zeta)^2$	0	$\frac{1}{4}\zeta(\sqrt{\zeta^2+12}-\zeta)-1$
C_{2-}	$-\frac{1}{6}\zeta(\sqrt{12+\zeta^2}+\zeta)$	$\frac{\sqrt{12+\zeta^2}+\zeta}{2\sqrt{3}}$	-1		0	$-\frac{1}{6}\zeta(\sqrt{12+\zeta^2}+\zeta)$	$\frac{1}{12}(\sqrt{\zeta^2+12}+\zeta)^2$	0	$-\frac{1}{4}\zeta(\sqrt{\zeta^2+12}+\zeta)-1$
D	$\frac{2}{3}$	$\frac{1}{\sqrt{3}}$	$\frac{\zeta}{2}$	$\zeta \neq 0, Q \neq \pm 1$	0	$\frac{8}{3\zeta^2}$	$\frac{4}{3\zeta^2}$	$1 - \frac{4}{\zeta^2}$	0
L_{1+}	0	0	1		1	0	0	0	$\frac{1}{2}(1+3\omega)$
L_{2+}	1	0	1		0	1	0	0	$\frac{1}{2}$
L_{1-}	0	0	-1		1	0	0	0	$\frac{1}{2}(1+3\omega)$
L_{2-}	1	0	-1		0	1	0	0	$\frac{1}{2}$
P_+	$\tilde{\Omega}_\lambda \leq 1$	0	1	$\omega = 0$	$1 - \Omega_\lambda$	$\Omega_\lambda \leq 1$	0	0	$\frac{1}{2}$
P_-	$\tilde{\Omega}_\lambda \leq 1$	0	-1	$\omega = 0$	$1 - \Omega_\lambda$	$\Omega_\lambda \leq 1$	0	0	$\frac{1}{2}$

TABLE IV: Eigenvalues and stability of fixed points of the dynamical system (17)-(20) for the inverse square potential. In the formulas below we have defined $\xi_\pm(\zeta) = \zeta^2 \pm \zeta\sqrt{\zeta^2+12}+12\omega$.

Label	λ_1	λ_2	λ_3	Dynamical Character
C_{1+}	$-\frac{3((1-\omega)\zeta+\sqrt{24(1+\omega)^3+(1+3\omega)^2\zeta^2})}{4\zeta}$	$-\frac{3((1-\omega)\zeta-\sqrt{24(1+\omega)^3+(1+3\omega)^2\zeta^2})}{4\zeta}$	$1+3\omega$	saddle
C_{1-}	$\frac{3((1-\omega)\zeta+\sqrt{24(1+\omega)^3+(1+3\omega)^2\zeta^2})}{4\zeta}$	$\frac{3((1-\omega)\zeta-\sqrt{24(1+\omega)^3+(1+3\omega)^2\zeta^2})}{4\zeta}$	$-(1+3\omega)$	saddle
C_{2+}	$-\frac{3}{8}(\xi_-(\zeta)+8(1-\omega)+\frac{1}{3} \xi_-(\zeta))$	$-\frac{3}{8}(\xi_-(\zeta)+8(1-\omega)-\frac{1}{3} \xi_-(\zeta))$	$-2+\frac{1}{2}\zeta(-\zeta+\sqrt{\zeta^2+12})$	attractor ($\zeta < 2$), saddle ($\zeta > 2$)
C_{2-}	$\frac{3}{8}(\xi_+(\zeta)+8(1-\omega)-\frac{1}{3} \xi_+(\zeta))$	$\frac{3}{8}(\xi_+(\zeta)+8(1-\omega)+\frac{1}{3} \xi_+(\zeta))$	$2+\frac{1}{2}\zeta(\zeta+\sqrt{\zeta^2+12})$	repulsor
D	$1-\frac{\zeta}{2}$	$-1-\frac{\zeta}{2}$	$-\frac{1}{2}\zeta(1+3\omega)$	saddle for $-2 < \zeta < 2$
L_{1+}	3ω	$\frac{3(1+\omega)}{2}$	$1+3\omega$	unstable
L_{2+}	1	-3ω	$\frac{3}{2}$	unstable for $\omega = 0$, saddle for $\omega \neq 0$
L_{1-}	-3ω	$-\frac{3}{2}(1+\omega)$	$-(1+3\omega)$	
L_{2-}	-1	3ω	$-\frac{3}{2}$	saddle for $\omega \neq 0$
P_+	0	$\frac{3}{2}$	1	unstable
P_-	0	$-\frac{3}{2}$	-1	

To identify an attractor, it should be noted that the points C_{2+}, L_{1-}, P_- , and, under certain circumstances, some points at infinity can act as attractors.

To understand the global nature of the model, it is necessary essentially to make a conformal compactification of the entire phase space of the solutions. The critical points at infinity can be identified by projecting onto the Poincaré sphere, as outlined in appendix C. In this case, the given projection is necessary, as it reveals significant contributions to the system's dynamics, including predominantly saddle behavior and the potential presence of attractors.

Now, it is convenient to write the dynamical equations as:

$$\tilde{\Omega}'_\lambda = \hat{P}(\tilde{\Omega}_\lambda, \beta, Q), \quad \beta' = \hat{Q}(\tilde{\Omega}_\lambda, \beta, Q), \quad Q' = \hat{R}(\tilde{\Omega}_\lambda, \beta, Q), \quad (21)$$

where \hat{P} , \hat{Q} and \hat{R} are polynomial functions of the dynamical variables. Since Q is compact, it is enough to project only the variables $\tilde{\Omega}_\lambda$ and β on the Poincaré sphere. Therefore, we define the following coordinates on the Poincaré sphere:

$$X = \frac{\tilde{\Omega}_\lambda}{\sqrt{1+\tilde{\Omega}_\lambda^2+\beta^2}}, \quad Y = \frac{\beta}{\sqrt{1+\tilde{\Omega}_\lambda^2+\beta^2}}, \quad Z = \frac{1}{\sqrt{1+\tilde{\Omega}_\lambda^2+\beta^2}}. \quad (22)$$

So at infinity ($Z \rightarrow 0$), the dynamical system has the form:

$$\begin{aligned} X' &= -Y(X\hat{Q}^* - Y\hat{P}^*), \\ Y' &= X(X\hat{Q}^* - Y\hat{P}^*), \\ Q' &= \hat{R}^*, \end{aligned} \quad (23)$$

where the polynomials \hat{P}^* , \hat{Q}^* and \hat{R}^* are given by:

$$\begin{aligned}\hat{P}^* &= \sqrt{3}zY^3 - 3(1+\omega)QXY^2, \\ \hat{Q}^* &= -\frac{3}{2}(1+\omega)QY^3, \\ \hat{R}^* &= \frac{3}{2}(1+\omega)(1-Q^2)Y^2.\end{aligned}\tag{24}$$

Therefore, the critical points/lines (X, Y, Q) at infinity are:

P_1 : $(\pm 1, 0, Q)$, which corresponds to critical lines

P_2 : $(-\cos\theta, \sin\theta, -1)$ and its antipodal $(\cos\theta, -\sin\theta, -1)$

P_3 : $(\cos\theta, \sin\theta, 1)$ and its antipodal $(-\cos\theta, -\sin\theta, 1)$

where $\theta = \arctan\left(\frac{\sqrt{3}(1+\omega)}{2\zeta}\right)$. However, it is straightforward to verify that only the critical line P_1 : $(-1, 0, Q)$ is located within the physical space $\tilde{\Omega}_\lambda \leq 1 - \beta^2$. Nevertheless, analysis of the dynamics near this line is rather difficult because, owing to either the compactified variables or the time rescaling, the compactification can end up canceling the dynamics of those components not at infinity. Graphically, however, the variables not projected on the Poincaré sphere show dynamics. This should be interpreted as indicating that the variables with canceled dynamics will undergo slower evolution than those without. Therefore, the equations are analyzed with the aid of graphics the better to understand and visualize these dynamics.

In Fig. 4 we plot the global phase portrait of the dynamical system for $\kappa\gamma^{1/2} = 4/3$. This figure shows that the phase space is divided into two halves, one corresponding to a contracting epoch ($Q < 0$) and the other to an expanding epoch ($Q > 0$). The dynamical system is bounded by the $Y = 0$ ($\beta = 0$), $Q = \pm 1$, and $\tilde{\Omega}_\rho = 0$ invariant submanifolds. Some trajectories which are past asymptotic to the matter dominated critical line P_+ with a sufficiently small value of Ω_ϕ after some expansion enter the contracting phase space and collapse to a big crunch at P_- . Conversely, models starting from P_+ with a large enough value of Ω_ϕ evolve to the future attractor C_{2+} , which represents a solution dominated by dark matter and dark energy, exhibiting acceleration for $\zeta < 2$ (Table III). There are trajectories past asymptotic to C_{2-} that evolve to C_{2+} . Other trajectories past asymptotic to C_{2-} enter the contracting phase space and recollapse to a big crunch at P_- . Additionally, we observe trajectories that approximate to the uniformly expanding solution, point D with coordinates $X = 1/2$, $Y = \sqrt{3}/4$, $Q = \zeta/2$, and then collapse to a big crunch. Note that points C_{2+} , C_{2-} and D lie on the $\rho = 0$ boundary. On this boundary, there exists a trajectory, among others, that is past asymptotic to point C_{2-} and evolves to D .

For the case $\omega = 0$, the analysis presented below, it is concluded that the system will exhibit saddle behavior with the critical point at $(Q, X, Y) = (\pm 1, -1, 0)$. However, it is important to note that the possibility of a small and constant β is also contained within this critical point. In particular, for $\beta < \frac{1}{\sqrt{3}}$ and under certain circumstances, such as $\zeta > 0$ and $Q < 0$, $Q' < 0$ will occur, causing $(Q, X, Y) = (-1, -1, 0)$ to act as an attractor, while the point $(Q, X, Y) = (1, -1, 0)$ in this example would require even more specific conditions and could act as a repulsor. The necessary conditions for the attractor and repulsor behavior will not be further explored, but it can be shown from a simple analysis of the equations. It suffices to conclude that the system truly exhibits critical behavior at the points $(Q, X, Y) = (\pm 1, -1, 0)$ and can exhibit saddle behavior or attractor and repulsor behavior, respectively, for the points $Q = -1$ and $Q = 1$, depending on the initial conditions of the solution. On the other hand, for $\omega = 1/3$, the points act as saddles, with $Q = \pm 1$ representing the real critical points. Based on this observation, it is possible to say that there will be two main trajectories, both interacting with the saddle points but in different directions. Additionally, there might be a third type of trajectory that undergoes a change in direction. It is unlikely that trajectories leading to attractor–repulsive points will emerge, and the analysis conducted so far lacks the capability to demonstrate or visualize such occurrences.

To analyze the variations, it is convenient to perform the projection described in appendix D, given that Q varies slowly in relation to Ω_λ , and β , and ζ remains constant. The following change of variable is considered:

$$\xi = -\frac{Y}{X}, \quad \chi = -\frac{Z}{X}.\tag{25}$$

For these variables and $\omega = 0$ the system of equations is the following:

$$Q' = \frac{1}{2}(1 - Q^2)(3\xi^2 - \chi^2), \quad \xi' = \frac{1}{2}\xi \left(3Q(\chi^2 + \xi^2) + \sqrt{3}\zeta\xi(2\xi^2 - \chi) \right), \quad \chi' = \chi\xi^2 \left(3Q + \sqrt{3}\zeta\xi \right), \tag{26}$$

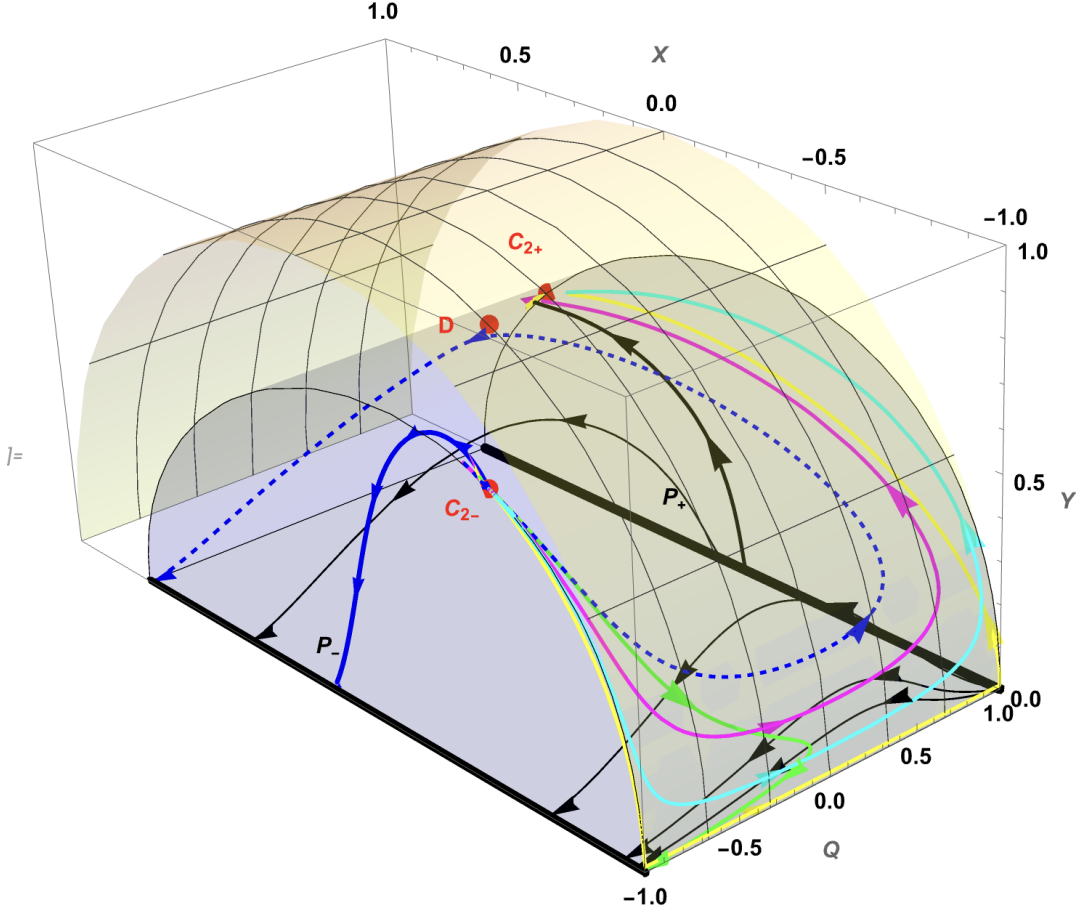


FIG. 4: Global phase portrait for the inverse square potential with $\zeta = 3/2$. The solutions of the system are C_{2+} , C_{2-} , D , P_+ , P_- and the points $X = -1$, $Y = 0$, $Q = \pm 1$. Some trajectories starting from the matter-dominated critical line P_+ converge asymptotically to C_{2+} , which represents a solution dominated by dark matter and dark energy. We also observe trajectories starting from the contracting solution C_{2-} which converge to the point C_{2+} . In addition, some trajectories after some expansion begin contracting and collapse to a big crunch at P_- .

and the variation matrix for the line $(-1, 0, Q)$ is null; therefore, its eigenvalues are null and correspond to a degenerate line that will be analyzed according to the method exposed in appendix E. Now note that the solution is independent of Q , so it should not show dynamics in the neighborhood (remember that in this context it means that it varies more slowly than the other variables), so we could consider it as a constant, just as ζ for the potential is constant. Using the angular equation in the neighborhood of interest, it is possible to see that the solutions are $\theta = 0, \pi/2$, and additionally, for $\frac{\zeta}{Q} < 0$, the solution is $\theta = \frac{1}{2} \text{arccot} \left(-\frac{\zeta}{2\sqrt{3}Q} \right)$. So, reviewing the radial equation in the neighborhood, it is possible to evaluate the behavior (if the radial component is also canceled, the analysis must be discarded as insufficient). Therefore, for the last solution it can be said that it is:

- repulsive for $Q > 0$ and $\zeta < 0$.
- attractive for $Q < 0$ and $\zeta > 0$.

the $\theta = 0$ solution is:

- repulsive for $Q > 0$.
- attractive for $Q < 0$.

and the $\theta = \pi/2$ solution does not exhibit radial dynamics. At this order the radial behavior is annulled, so higher-order terms must be considered; however, graphically it can be seen that the evolution is angular and not radial, so it is discarded.

As previously mentioned, it is still necessary to assess the dynamics of the variable Q and not disregard it. It is easy, then, to see that for large β , $Q' > 0$.

Equivalently, for $\omega = 1/3$, the equations are:

$$\begin{aligned} Q' &= \frac{1}{2}(1 - Q^2)(4\xi^2 - 2\chi^2 - \chi), \\ \xi' &= \frac{1}{2}\xi \left(Q(4\xi^2 + 2\chi^2 - \chi) + \sqrt{3}\zeta\xi(2\xi^2 - \chi) \right), \\ \chi' &= \sqrt{3}\zeta\xi^3\chi - Q\chi(\chi + \chi^2 - 4\xi^2). \end{aligned} \quad (27)$$

The variation matrix for the analyzed point have null eigenvalues, so its structure is evaluated using polar coordinates (see appendix E). From this, the conclusions are slightly more difficult to analyze analytically. Firstly, in the plane (ξ, χ) the angles $\theta = 0, \pi/2$ are obtained, then its dynamics will be the following:

1. For $\theta = 0$, the solution is:

- attractive for $Q > 0$.
- repulsive for $Q < 0$.

2. For $\theta = \pi/2$, the solution is

- repulsive for $Q > 0$.
- attractive for $Q < 0$.

Secondly, it is necessary to note that the sign of Q' will be described such that $\text{sign}(Q') = \text{sign}(4\xi^2 - 2\chi^2 - \chi)$. This expression also seems to divide the regions of influence of the different behaviors

2. Exponential potential

Now, we consider the potential $V(\phi) = V_0 e^{-\alpha\phi}$. For this potential we find $\mu(\zeta) - 3/2 = -1/2$; therefore, the points C_{1+} , C_{1-} , C_{2+} , C_{2-} and D listed in Table I do not manifest in the phase space for this model. All the remaining points/lines correspond to non-accelerating solutions, with the exception of point B_+ , which represents a saddle de Sitter point dominated by the mimetic field. This point exhibits unstable behavior in the ζ direction. Point B_- is the contracting analogue of B_+ . However, it is worth noting that the invariant submanifold $\zeta = 0$ divides the phase space into two regions, thus preventing trajectories from crossing between them. From Eq. (20), we deduce that if $\mu(\zeta) - 3/2 < 0$ as $\zeta \rightarrow 0$, then $\zeta' > 0$ and point B_+ acts as a future attractor for trajectories in the region $\zeta < 0$.

No attempt will be made to make graphics that describe the solutions in 4-dimensional space, since, regardless of the method for this, it might not be visual enough to be interpreted. However, it is possible to have some degree of understanding by analyzing the invariant submanifolds and extrapolating the behavior to their neighborhoods. That being said, the $\zeta = 0$ and $\beta = 0$ manifolds have a general qualitative behavior independent of the shape of the potential, so their behaviors are similar to that described in subsection III B, added to the analysis of the $\hat{\Omega}_\rho = 0$ submanifold, which it is now possible to analyze since the potential is known. For this potential, the variable ζ is given by $\zeta = \frac{\alpha}{\kappa\sqrt{V}}$, with $V = V_0 e^{-\alpha t}$. Therefore, $\alpha < 0$ implies $\zeta < 0$, and $\zeta \rightarrow 0$ when $t \rightarrow \infty$. However, $\alpha > 0$ implies $\zeta > 0$, and $\zeta \rightarrow \infty$ when $t \rightarrow \infty$, it being necessary to consider the critical points at infinity.

The critical points and their respective dynamics in the manifold are then detailed in Figs. 5 and 6:

- For both values of ω : B_+ exhibits saddle behavior for centre manifold, with $\zeta > 0$ representing the unstable direction, and B_- shows saddle behavior for centre manifold, with $\zeta < 0$ as the stable direction. However, as previously mentioned, the point B_+ behaves as an attractor for trajectories in the region $\zeta < 0$, while manifesting saddle behavior for trajectories in the region $\zeta > 0$, and only the ζ direction is unstable.
- For $\omega = 0$: A_2 displays saddle behavior, but A_2 is a line where one of its ends touches the submanifold, since we are interested in the neighborhood it must be considered, so, the influence on the subsystem is minimal, P_+ shows repulsive behavior in directions other than the critical axis, while P_- is the contracting analogue of P_+ .

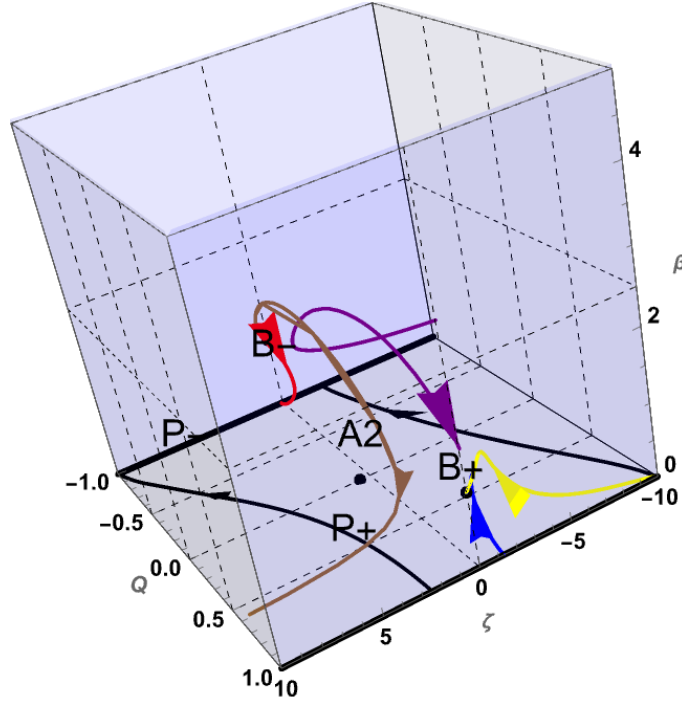


FIG. 5: Phase portrait of the invariant submanifold $\tilde{\Omega}_\rho = 0$ for $\omega = 0$. Some trajectories in the region $\zeta < 0$ starting from the matter dominated critical line P_+ as $\tau \rightarrow -\infty$ converge to the dark energy dominated point B_+ as $\tau \rightarrow \infty$. In the region $\zeta > 0$ we observe trajectories that evolve to some critical point at $\zeta \rightarrow \infty$. Also, there are trajectories which are past asymptotic to P_+ and collapse to a big crunch at P_- .

- For $\omega = 1/3$: L_{2+} exhibits repulsive behavior in directions other than the critical axis, L_{2-} exhibits attractive behavior in directions other than the critical axis, and A_1 shows saddle behavior. It is important to note that A_1 is a curve where one of its ends touches the submanifold, as we are interested in the neighborhood it must be considered, so, the influence on the subsystem is minimal.

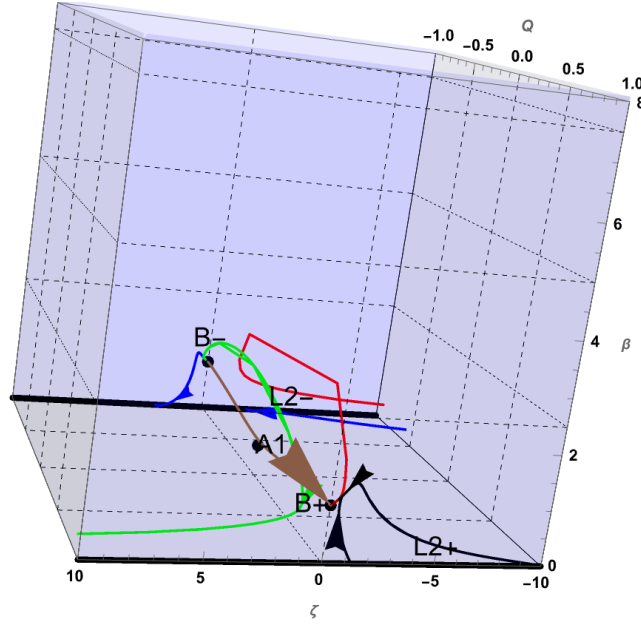


FIG. 6: Phase portrait of the invariant submanifold $\tilde{\Omega}_\rho = 0$ for $\omega = 1/3$. Some trajectories in the region $\zeta < 0$ starting from the dark matter dominated critical line L_{2+} as $\tau \rightarrow -\infty$ converge to the dark energy dominated point B_+ as $\tau \rightarrow \infty$. In the region $\zeta > 0$ we observe trajectories that evolve to some critical point at $\zeta \rightarrow \infty$.

The stability in the $\tilde{\Omega}_\rho$ axis does not exhibit a unique behavior throughout the submanifold and, since this term depends on ρ and D , the analysis is not easy. It is evident, however, that the submanifold is inaccessible from an external point since ρ must be null for this, so it is possible only if ρ is null by default.

The critical points at infinity can be found by projecting the variables $\tilde{\Omega}_\lambda, \beta, \zeta$ on the Poincaré sphere, see appendix C. In this case the procedure applied above is generalizable. Here, the equations have the particularity that $\mu(\zeta) = 1$, and the coordinates on the Poincaré sphere are given by:

$$\begin{aligned} X &= \frac{\tilde{\Omega}_\lambda}{\sqrt{1 + \tilde{\Omega}_\lambda^2 + \beta^2 + \zeta^2}}, \quad Y = \frac{\beta}{\sqrt{1 + \tilde{\Omega}_\lambda^2 + \beta^2 + \zeta^2}}, \\ Z &= \frac{\zeta}{\sqrt{1 + \tilde{\Omega}_\lambda^2 + \beta^2 + \zeta^2}}, \quad W = \frac{1}{\sqrt{1 + \tilde{\Omega}_\lambda^2 + \beta^2 + \zeta^2}}. \end{aligned} \quad (28)$$

At infinity ($W \rightarrow 0$), the dynamical system transforms to:

$$\begin{aligned} X' &= \sqrt{3}Y^3Z(Y^2 + Z^2), \\ Y' &= -\sqrt{3}XY^4Z, \\ Z' &= -\sqrt{3}XY^3Z^2, \\ Q' &= 0, \end{aligned} \quad (29)$$

we have omitted showing the form of the functions for each derivative after the projection, for simplicity. In the same way as before, the solution inside of the physical space (X, Y, Z, Q) can be described as $P_4 : (X, 0, Z, Q)$, with the condition $X^2 + Z^2 = 1$.

Once again, it becomes evident that the variable Q will be eliminated in the limit as $W \rightarrow 0$, as it is not included in the set of the projected variables. Despite this, a thorough analysis of the equations will be conducted and supported by graphics for enhanced comprehension. On the other hand, it is easy to notice that the solution is indifferent to the values of X, Z , which, if it is part of the coordinates in the Poincaré sphere, implies a lack of dynamics in those directions locally, mainly on Z since X is associated with $\tilde{\Omega}_\lambda$ and this must still respond to the limitations of the physical phase space.

Accordingly, to analyze the variations, it is convenient to carry out the projection described in appendix D since Q varies slowly with respect to $\tilde{\Omega}_\lambda$, β and ζ . A priori, we considered a new projection tangent to $(Q, X, Y, Z) = (Q, -1, 0, 0)$. However, the results were inconclusive, generally indicating some unstable directions and lacking a clear pattern in the relationship between these variables and Q .

However, in this analysis, taking into consideration the choice made for the point in the tangential space, the points $(Q, X, Y, Z) = (Q, 0, 0, \pm 1)$ have been left out, despite the expectation that the behavior described in the analysis could be extrapolated to these points. However, it is anticipated that this is not the case.

It is possible to make a projection in the tangential space at $Z = 1$ (it is enough to analyze only one point since $Z = -1$ is its antipode). This analysis is important because this point appears to be graphically significant for the system and is also relevant for curves that are compatible with our universe. To go directly from the original coordinates to the final ones, the following relations are used:

$$Q = Q, \quad \tilde{\Omega}_\lambda = \chi/\epsilon, \quad \beta = \xi/\epsilon, \quad \zeta = 1/\epsilon. \quad (30)$$

Rewriting the equations in these new variables with the respective time rescaling (which is evident when explicitly written), it is found that the variation matrix is null, which indicates a degenerate point. The procedures detailed in appendix E for slightly degenerate points are applied. Unfortunately, these procedures do not provide detailed insights into the structures around this point; we therefore proceed to show graphics around these points, where in the new variables they correspond to the points $(Q, \chi, \xi, \epsilon) = (Q, 0, 0, 0)$, see figure 7.

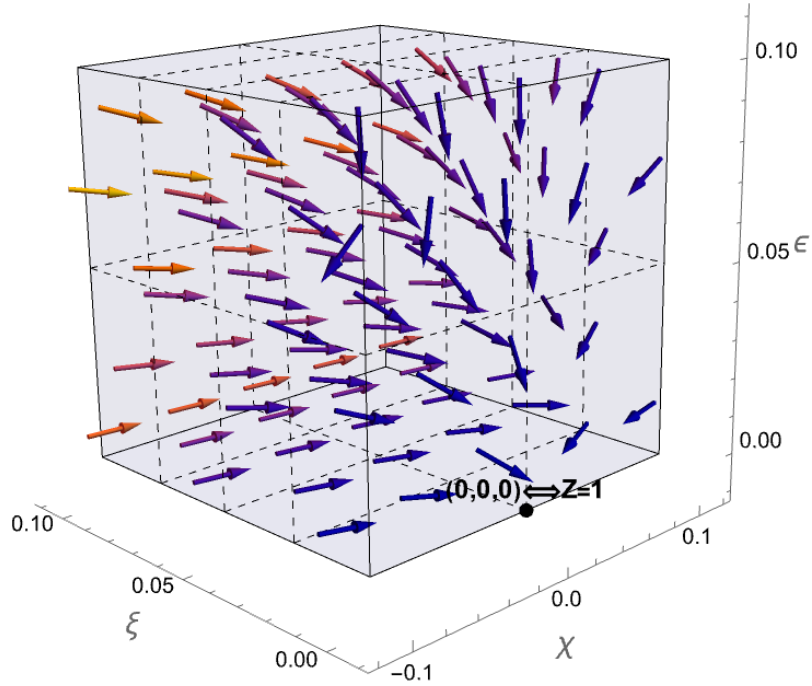


FIG. 7: Behavior around the point $Z = 1$ for $\omega = 0, 1/3$. Note that the graphic is independent of the values of ω and Q .

Is possible to see an attractive behavior in all the components, except for Q , which requires a separate analysis.

It is worth noting from Eqs. (17)-(20) with $\omega = 0$ that the $\tilde{\Omega}'_\lambda$ equation decouples. This leads to a three-dimensional reduced dynamical system for the variables Q , ζ and β . So it is possible to graph the global phase space of this reduced dynamical system. By projecting the coordinates ζ and β on the Poincaré sphere we define:

$$X = \frac{\zeta}{\sqrt{1 + \beta^2 + \zeta^2}}, \quad Y = \frac{\beta}{\sqrt{1 + \beta^2 + \zeta^2}}, \quad Z = \frac{1}{\sqrt{1 + \beta^2 + \zeta^2}}. \quad (31)$$

In Fig. 8 we plot the global phase space of the reduced dynamical system characterized by the coordinates Q , X and Y for the exponential potential. The phase space is divided into two halves, one corresponding to a contracting epoch ($Q < 0$) and the other representing an expanding epoch ($Q > 0$). We can see that, for different values of X , some trajectories which are past asymptotic to the matter-dominated critical line P_+ , with a sufficiently small value of Ω_ϕ after some expansion enter the contracting phase space and collapse to a big crunch at P_- . By way of contrast, in the region $X < 0$ ($\zeta < 0$), there are models starting from P_+ with a large enough value of Ω_ϕ that evolve to the future attractor B_+ , which represents an expanding de Sitter accelerated solution dominated by the mimetic field. In the region $X > 0$ ($\zeta > 0$), there are models starting from P_+ with a large enough value of Ω_ϕ that approximate to the point B_+ , evolve to the point $X = 1, Y = 0, Q = 1$ (note that $X = 1$ coincides with $Z = 1$ in the previous analysis) at infinity, and then move to the point $X = 1, Y = 0, Q = -1$. Also, in $X > 0$, we observe trajectories that are past asymptotic to B_- and evolve to the point $X = 1, Y = 0, Q = -1$ at infinity. There are trajectories which are past asymptotic, as well as future asymptotic to the Einstein static solution A_2 , characterized by coordinates $X = 0, Y = 1/2, Q = 0$.

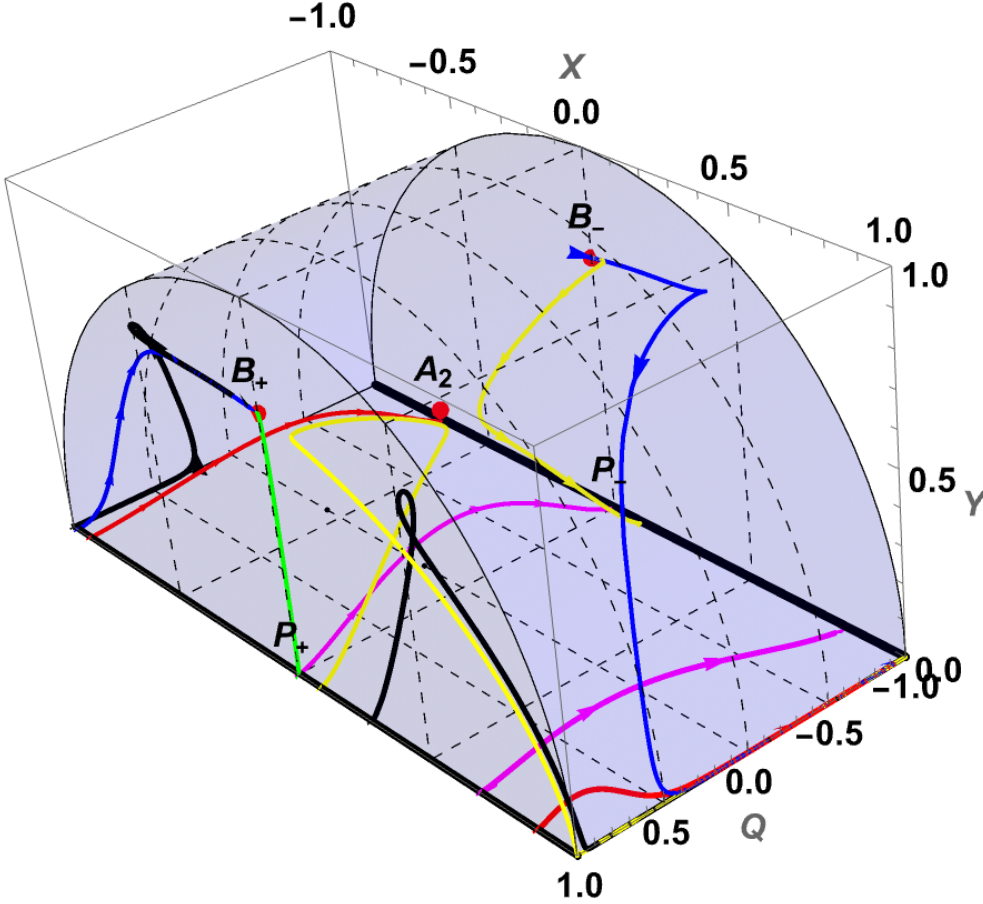


FIG. 8: Global phase portrait of the reduced dynamical system for an exponential potential with $\omega = 0$. The solutions of the system are B_+ , B_- , A_2 , P_+ , P_- and the points $X = 1, Y = 0, Q = \pm 1$. Some trajectories in the region $X < 0$ ($\zeta < 0$) which are past asymptotic to the matter dominated critical line P_+ evolve to the mimetic field dominated point B_+ . Some trajectories in the region $X > 0$ ($\zeta > 0$) which are past asymptotic to the matter-dominated critical line P_+ evolve to the critical point at infinity $X = 1, Y = 0, Q = 1$ and then move to $X = 1, Y = 0, Q = -1$. Also, there are trajectories that, after some expansion, begin contracting and collapse to a big crunch at P_- . Moreover, the green curve has been added based on the parameters for the exponential potential obtained from the combined *PaSNe + OHD* dataset, as listed in Table VI. This curve represents accelerated expansion that seems to end in a de Sitter solution. However due to numerical accuracy limitations, it is only possible to represent the segment from P_+ to B_+ . Due to instability in this direction, the curve is expected to move towards $(Q, X, Y) = (1, 1, 0)$, which represents a similar solution. Finally, the transition to $Q = -1$ is not observed, and based on the evaluation of Figure 9, it does not appear to occur.

In this context, it can be demonstrated that in the vicinity of infinity (where $X = 1$ in the last-defined coordinates), $Q' < 0$ holds for any Q , indicating that only $(Q, X, Y) = (-1, 1, 0)$ would act as an attractor, while $(Q, X, Y) = (1, 1, 0)$ would be a saddle point. There are special conditions in which $Q' > 0$ can be added, but they are transient. To understand this, it must be taken into account that the form of Q and the temporal rescaling suggest that the submanifolds $Q = \pm 1$ are inaccessible, so we eventually return to the first case. In summary, some curves may experience a transitory asymptotic approach to $(Q, X, Y) = (1, 1, 0)$ of long duration. However, this may not be numerically appreciable since, as previously mentioned, $Q = 1$ is an invariant submanifold, and, owing to lack of precision, a point in the vicinity might be approached as one of the submanifolds. The next analysis provides a thorough exploration of the behavior of the system:

$$Q' = (1 - Q^2) \frac{3\beta^2 - 1}{2} \quad \Delta_Q \quad 0 \\ 3\beta^2 - 1 \quad \Delta_Q \quad 0 \\ \beta^2 \quad \Delta_Q \quad 1/3$$

Here, Δ denotes some inequality sign, and ∇ its inversion, and

$$\beta' = -\frac{\sqrt{3}}{2}\beta^2\zeta - \frac{3}{2}\beta Q(\beta^2 - 1) \quad \Delta_\beta \quad 0 \\ -\beta\zeta - \sqrt{3}Q(\beta^2 - 1) \quad \Delta_\beta \quad 0 \\ \beta\zeta + \sqrt{3}Q(\beta^2 - 1) \quad \nabla_\beta \quad 0 \\ \zeta \quad \nabla_\beta \quad -\sqrt{3}Q\frac{\beta^2 - 1}{\beta}.$$

We indicate that:

- Assuming that β is finite (in this context, $\beta \ll \zeta$), then $\nabla_\beta \rightarrow >$ implies $\Delta_\beta \rightarrow <$, which in turn implies $\beta' < 0$. Therefore, with sufficient time at infinity, $\beta^2 < 1/3 \Rightarrow \Delta_Q \rightarrow <$, leading to $Q' < 0$.
- If we consider β as a variable at infinity (assuming it is in the vicinity of $(X, Y) = (1, 0)$, so in the best-case scenario $\beta \gg 0$ and $\beta \ll \zeta$), then:

$$\zeta \quad \nabla_\beta \quad -\sqrt{3}Q\beta + \dots$$

Then, under the assumption of being in the mentioned neighborhood, it must hold that $\nabla_\beta \rightarrow >$. Following the same reasoning as in the previous point, this implies $\beta' < 0$. With sufficient time, $\beta^2 < 1/3$, and consequently, $Q' < 0$. Note that the second condition may not be very evident, but by contradiction, if it is assumed that $\zeta \propto \beta$, it is straightforward to conclude that $(X, Y) \neq (1, 0)$.

- Still, there appears to be one apparent option, and it arises when noticing that the inequality expression to evaluate for ζ diverges at $\beta = 0$. However, if enough time has elapsed for $Q < 0$, then the expression will transform back to $\zeta > -\infty$, thus recovering the previous conclusions. If the assumption about Q is not true, perhaps some point in finite space could be dominating the trajectory; however, the curves seem to indicate the opposite.

This brief analysis does not constitute a formal proof but rather provides arguments to estimate its behavior. Therefore, the possibility that some trajectory asymptotically approaches $Q = 1$ should not be ruled out. Unfortunately, numerical evaluation does not yield significantly better results.

3. Bounce behavior

Regarding the possibility of finding bounce-type solutions, we could consider universes that contract and then expand. It is necessary to evaluate the possibility of this behavior. To do so, one can pay special attention to the transitions from contraction to expansion solutions; several examples of this can be found in Article [45]. Specifically, these universes would have $(a, \dot{a}, \ddot{a}) = (\text{positive}, \text{negative or } -\infty, \text{preferably positive})$ initially and end with $(a, \dot{a}, \ddot{a}) = (\text{positive}, \text{positive or } \infty, \text{preferably positive})$. In some specific cases, we observe curves satisfying $Q = -1 \rightarrow Q = 1$, which are good candidates for the aforementioned conditions and will be analyzed in conjunction with the other variables they might imply.

It is important to note that the time transformation $d\tau = Ddt$ allows the parameter τ to potentially diverge when $a = 0$ or $\dot{a} = \pm\infty$. Consequently, a bouncing solution might not be fully represented if any of the above conditions are met. Moreover, it is known that bounce-type solutions are not possible in certain scenarios, such as those discussed in the article [46]. However, in this specific case, the presence of positive curvature and the possibility of the scalar field (acting as dark matter) to violate the weak energy condition are considered. These conditions make the manifestation of bounce behaviour possible.

In addition to considering the variable $Q(\tau)$, we should also examine the variable $\beta(\tau)$. Assuming that we know both $Q(\tau)$ and $\beta(\tau)$ for a given curve for all τ –at least numerically– it is possible to determine the behaviour of the scale factor $a(\tau)$ for a general potential as follows:

$$a(\tau) = \frac{\sqrt{3k}}{\kappa} \frac{1}{\sqrt{V(t(\tau))}} \frac{\beta}{\sqrt{1-Q^2}} \quad (32)$$

where $t = t(\tau)$ can be obtained by isolating D from the definition of β and then using it to solve $d\tau = Ddt$. This allows $t = t(\tau)$ to be determined. Consequently, the next step involves solving:

$$\int \frac{\sqrt{3}\beta}{\kappa} d\tau = \int \sqrt{V(t)} dt \quad (33)$$

In these expressions, the assumption that $a > 0$ has been made, allowing $\dot{a} = \dot{a}(Q)$ to be determined from the definition of Q . Although the specific form of $a(\tau)$ will depend significantly on the potential, it is natural to seek a bouncing solution that does not start at $a = 0$ (i.e., does not begin in contraction), and therefore, preferably does not start at $\beta = 0$.

Therefore, for specific cases:

- For the inverse square potential, the curves satisfying the conditions are the pink, cyan, and yellow curves. All of these curves transition from the points C_{2-} to the point C_{2+} .
- For the exponential potential, although it is more general, these curves are not directly visible. However, in the submanifold $\tilde{\Omega}_\lambda = 0$ (see Figs. 7 and 8), both curves going from point B_- to point B_+ and curves that approach or depart from infinity while passing near these points can be observed. In this case, it is necessary to evaluate $a(\tau)$ to confirm the behavior.

IV. MIMETIC FIELD POTENTIAL ANALYSIS

In this section we obtain numerical solutions for the differential equations, and explore the dynamics of the Hubble parameter and the scale factor for different mimetic field potentials. Moreover, we compare these solutions with those of the non-flat Λ CDM model.

It is useful to write the cosmological equations as function of redshift z to facilitate the comparison of the models with the observational data. The relationship between redshift and scale factor is given by:

$$1 + z = \frac{a(t_0)}{a(t)}, \quad (34)$$

where t_0 refers to the present time which will be set to zero. The derivative with respect to cosmic time of this expression results in:

$$\frac{dz}{dt} = -(1+z)H. \quad (35)$$

Expressed in terms of the parameter z , the second Friedmann equation can be written as:

$$\frac{dH}{dz} = \frac{3H}{2(1+z)} - \frac{\kappa^2}{2(1+z)H} V(t) - \frac{\Omega_k H_0^2 (1+z)}{2H}, \quad (36)$$

where $t = t(z)$ and the potential $V(t)$ is parametrically considered as $V(z)$. The function $t(z)$ is determined from the equation:

$$\frac{dt}{dz} = -\frac{1}{(1+z)H} \quad (37)$$

with the initial condition $t(0) = 0$. Additionally, the first Friedman equation (13) evaluated at the present time yields the following constraint among the density parameters:

$$1 = \Omega_{\rho,0} + \Omega_{\lambda,0} + \Omega_{\phi,0} + \Omega_{k,0}. \quad (38)$$

Here, the subscript 0 indicates that the respective density parameter is evaluated at the present time.

We analyze two family of models for the mimetic field potential. The first family comprises exponential potentials (EP) defined as $V(\phi) = V_0 e^{-\alpha\phi}$. The second involves inverse quartic potentials (IQP) expressed as $V(\phi) = V_0(1 + \delta\phi^2)^{-2}$. This potential with a fixed $\delta = 1$ was previously considered in Ref. [14] to construct solutions featuring a non-singular bounce in a contracting flat universe. By utilizing the definition of the density parameter Ω_ϕ , we establish the relationship between V_0 and the parameters H_0 and $\Omega_{\phi,0}$ as $V_0 = 3H_0^2\Omega_{\phi,0}$. In Figs. 9 and 10 we respectively plot the behavior of the Hubble parameter and the scale factor as a function of the dimensionless cosmic time $t \cdot H_0$. As initial conditions, we used $a_0 = 1$ and $H_0 = 67.74 \text{ km s}^{-1} \text{ Mpc}^{-1}$, and $\Omega_{\phi,0} = 0.6911$ and $\Omega_{k,0} = -0.001$ as the values of the density parameters at the present time. For illustration, we consider different values of α and δ for each family. We have also included the non-flat Λ CDM solution for comparison, which is analogous to setting $\alpha = 0$ of $\delta = 0$ in the potentials under consideration. The density parameter associated with radiation was not considered in the analysis. We observe that the solutions are consistent with late-time acceleration, and the deviation from the Λ CDM model increases when α or δ increases. The deviation of the models from Λ CDM is more sensitive to changes of the parameter α than δ . For the exponential potential, we see that the dynamical evolution of the system depends on the sign of the parameter α (Fig. 9), which agrees with the dynamical system analysis performed in Sec. (III C 2). The numerical solutions of Fig. 9 suggests that $H \rightarrow \infty$ for $\alpha < 0$, $H \rightarrow \text{constant}$ for $\alpha = 0$ and $H \rightarrow 0$ for $\alpha > 0$. In fact, for $\alpha < 0$, we observe that several trajectories in the region $X < 0$ evolve to the point B_+ (see Fig. 8), which corresponds to an accelerating solution dominated by the mimetic field $\Omega_\phi = 1$ and $H \rightarrow \infty$ when the trajectories approximate to B_+ in this region. For $\alpha > 0$ there are also trajectories in the region $X > 0$ that approximate to the point B_+ , but in this case $H \rightarrow 0$; however, the trajectories then approximate to the point $X = 1, Y = 0, Q = 1$ at infinity, and then go to the point $X = 1, Y = 0, Q = -1$. Analogously, for the inverse quartic potential, the evolution of the system depends on the sign of the parameter δ (see Fig. 10). The numerical solutions of Fig. 10 suggest that $H \rightarrow \infty$ for $\delta < 0$, $H \rightarrow \text{constant}$ for $\delta = 0$ and $H \rightarrow 0$ for $\delta > 0$. For this potential we obtain $\zeta = \frac{4\delta\phi}{\kappa V_0^{1/2}}$ with $1 + \delta\phi^2 > 0$, which shows that $\delta > 0$ implies $\zeta > 0$ and the potential $V(\phi) = V_0(1 + \delta\phi^2)^{-2}$ tends to zero and $\zeta \rightarrow \infty$ when $t \rightarrow \infty$. For $\delta < 0$ we note that the variable $\zeta < 0$ and the potential diverges at the times $t = \pm\sqrt{-1/\delta}$. We may infer from the general analysis of the dynamical system of section III for arbitrary potential that the trajectories evolve to the point C_{2+} , where $\Omega_\phi = 1$ and $H \rightarrow \infty$, and the solution represents a big rip.

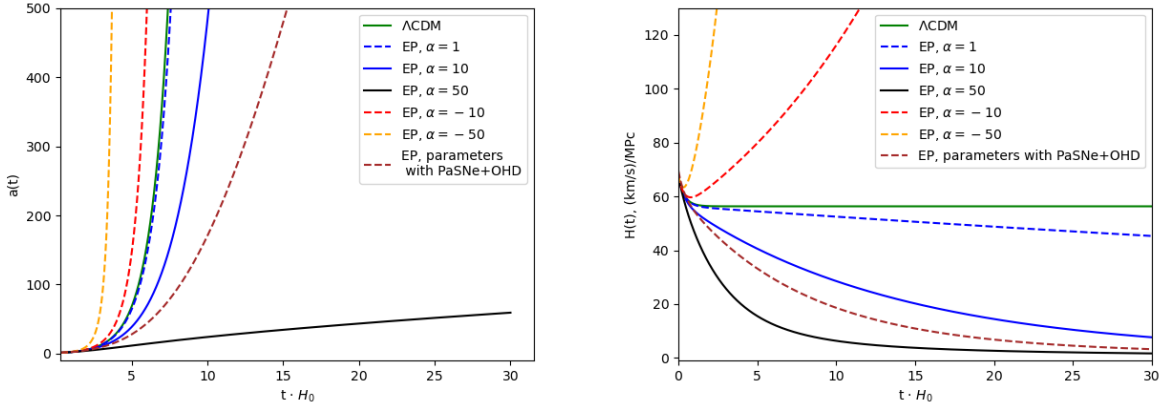


FIG. 9: $H(t)$ vs $t \cdot H_0$ (left panel) and $a(t)$ vs $t \cdot H_0$ (right panel) for the exponential potential with $\alpha = 1, 10, 50, -10, -50$. The dashed brown curves have been fully evaluated using the parameters from Table VI, i.e., $H_0 = 69.49$, $\alpha = 18.48$, $\Omega_{\phi,0} = 0.699$, $\Omega_{k,0} = -0.02$.

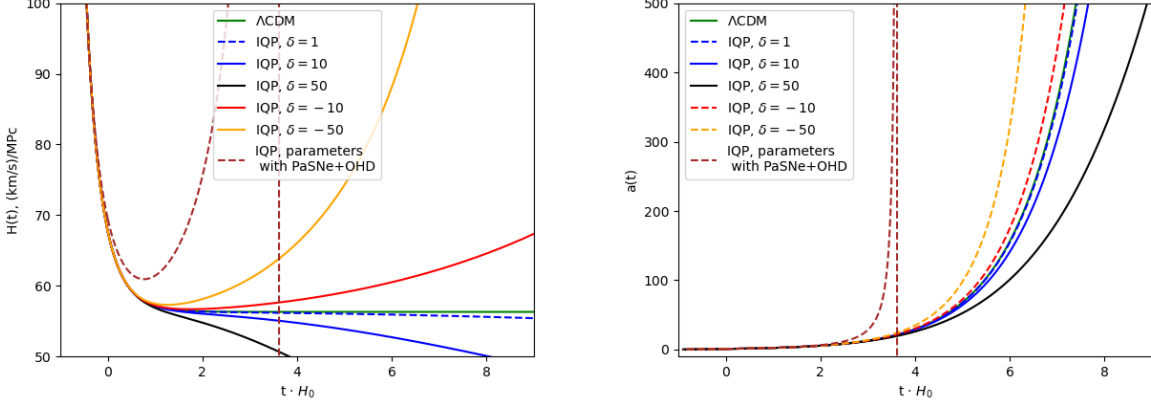


FIG. 10: $H(t)$ vs $t \cdot H_0$ (left panel) and $a(t)$ vs $t \cdot H_0$ (right panel) for the inverse quartic potential with $\delta = 1, 10, 50, -10, -50$. The dashed brown curves have been fully evaluated using the parameters from Table VI, i.e., $H_0 = 69.41$, $\delta = -368.8$, $\Omega_{\phi,0} = 0.696$, $\Omega_{k,0} = 0.035$.

V. OBSERVATIONAL ANALYSIS

This section is devoted to exploring the parameter space of the cosmological models proposed in section IV using public available observational data. To this end, the Observational Hubble Database from the cosmic chronometers [OHD, 47] and the Pantheon database for Type Ia supernovae [PaSN, 48] are considered. The fit of the data is performed with a Bayesian statistical analysis using the algorithm called EMCEE [49], which implements an affine-invariant Markov Chain Monte Carlo (MCMC) sampler of the posterior distribution function (PDF) to minimize the following expression:

$$\ln \left(\mathcal{L}(\theta) \prod_j \mathcal{P}(\theta_j) \right) \propto -\frac{\chi^2(\theta)}{2} + \sum_j \ln(\mathcal{P}(\theta_j)) \quad (39)$$

where $\mathcal{L}(\theta)$ is the likelihood and $\mathcal{P}(\theta_j)$ identifies the prior imposed on the j th parameter. θ identifies the set of free parameters considered in the MCMC approach. The merit function, $\chi^2(\theta)$, depends on the differences between observed data (\mathbf{D}) and model predictions ($\mathbf{m}(\theta)$) over the redshift:

$$\chi^2(\theta) = (\mathbf{D} - \mathbf{m}(\theta))^T \mathbf{C}^{-1} (\mathbf{D} - \mathbf{m}(\theta)) \quad (40)$$

\mathbf{C} being the noise covariance matrix of the observed data. In this notation, \mathbf{D} and $\mathbf{m}(\theta)$ are vectors while \mathbf{C}^{-1} is the inverse matrix of \mathbf{C} . The value of each parameter and its uncertainty are obtained through marginalization of the posterior distribution function of each parameter, as the median (the 50th percentile) and recovering the 16th and 84th percentiles to provide respectively the upper and lower uncertainties.

Each cosmological model is tested with three merit functions that depends on the data set considered, which are based on the observational Hubble data only (OHD, χ_{OHD}^2), on the Pantheon data set data only (PaSNe, χ_{PaSNe}^2) and on a combination of the two (OHD+PaSNe, $\chi_{\text{OHD+PaSNe}}^2$). Concerning the simultaneous fit, the merit function is written as:

$$\chi_{\text{OHD+PaSNe}}^2(\theta) = \chi_{\text{OHD}}^2(\theta) + \chi_{\text{PaSNe}}^2(\theta) \quad (41)$$

for which we assume that measurements from different databases are uncorrelated. Details about χ_{OHD}^2 and χ_{PaSNe}^2 are presented in the next sections.

A. Data and modelling

1. The Observational Hubble Database

The Observational Hubble Database, OHD, consists of 51 measurements of the Hubble parameter that covers the redshift range 0.07–2.36 [47, 50], which are obtained from the differential age method [DA, 50, 51] and from the baryon acoustic oscillation measurements. These OHD values can be compared directly with our proposed cosmological models that yield $H(z; \Theta)$ solving equations (36) and (37) (section IV), with Θ being the set of cosmological parameters that define our proposed models. Although some correlation is expected for the BAO measurements owing to overlapping among the galaxy samples or the cosmological model dependence in the clustering estimation [see discussion in 47], we follow previous work that assume no correlation between these measurements [e.g. 52]. Therefore, the covariance noise matrix is diagonal (i.e. uncorrelated noise, $(\mathbf{C}^{-1})_{i,j} = \delta_{i,j}/\sigma_i^2$), and consequently the maximization of the posterior distribution is driven by the merit function:

$$\chi_{\text{OHD}}^2(\theta) = \sum_{i=1}^{51} \left(\frac{H_{\text{obs},i} - H(z_i; \theta)}{\sigma_{H_{\text{obs},i}}} \right)^2, \quad (42)$$

where $H_{\text{obs},i}$ and σ_{H_i} are respectively the observed Hubble parameter and its uncertainty at redshift z_i (OHD values). $H(z_i; \theta)$ is the Hubble parameter provided by the model at the redshift z_i , and θ is the set of free parameters. In this case, θ corresponds to the set of cosmological parameters, i.e. $\theta = \Theta$. In our implementation, we applied the explicit Runge-Kutta method of order 8 to obtain the solution of $H(z_i; \theta)$ for each point explored in the parameter space.

2. The Pantheon Supernovae Database

The Pantheon data set, PaSNe, contains the apparent magnitude of 1048 SNe Ia in the redshift range 0.01–2.3 [48]. These observational measurements are fitted to the apparent magnitude model, $m_b(z_i; \theta)$, which is written as [53–56]:

$$m_b(z_i; \theta) = 5 \log_{10} (D_L(z_i; \Theta)) + \mathcal{M}, \quad (43)$$

where \mathcal{M} is considered a nuisance parameter that encompasses elements such as the absolute magnitude M_{abs} , which acts as a calibration term of the apparent magnitude of the SNIa sample [see details in 53–56]. The (dimensionless) luminosity distance, $D_L(z_i; \Theta)$, depends on the cosmological model studied:

$$D_L(z_i; \Theta) = (1 + z_i) S_k \left(H_0 \int_0^{z_i} \frac{dz'}{H(z'; \Theta)} \right), \quad (44)$$

where

$$S_k(x) = \begin{cases} \frac{1}{\sqrt{-\Omega_{k,0}}} \sin(\sqrt{-\Omega_{k,0}}x) & \text{for } k = +1 \\ x & \text{for } k = 0 \\ \frac{1}{\sqrt{\Omega_{k,0}}} \sinh(\sqrt{\Omega_{k,0}}x) & \text{for } k = -1 \end{cases} \quad (45)$$

The variable Θ identifies the set of cosmological parameters of the proposed model. As in the previous section, a numerical approach is taken into consideration to generate the model. We compute the numerical solution of $D_L(z_i; \Theta)$ for each Θ and z_i , for which the explicit Runge-Kutta method of order 8 is applied to Eqs. (36), (37) and to the derivative of the luminosity distance:

$$\frac{d}{dz} D_L(z; \Theta) = \frac{D_L(z; \Theta)}{1+z} + \frac{H_0 (1+z)}{H(z; \Theta)} \sqrt{1 + \Omega_{k,0} \left(\frac{D_L(z; \Theta)}{(1+z)} \right)^2}, \quad (46)$$

which is valid for every value of k ($k = -1, 0, 1$). Once the solution of $D_L(z_i; \Theta)$ for each z_i is achieved, the apparent magnitude model is established with the set of free parameters $\theta = \{\Theta, \mathcal{M}\}$. The merit function is then given by:

$$\chi_{\text{PaSNe}}^2(\theta) = (\mathbf{m}_{b,\text{obs}} - \mathbf{m}_b(\theta))^T \mathbf{C}^{-1} (\mathbf{m}_{b,\text{obs}} - \mathbf{m}_b(\theta)), \quad (47)$$

where $\mathbf{m}_{b,\text{obs}}$ and $\mathbf{m}_b(\theta)$ are vectors containing respectively the observed and theoretical apparent magnitudes of the whole SNe Ia sample. For the Pantheon measurements, the covariance matrix \mathbf{C} depends on both a statistical and

a systematic component describing the uncertainties; i.e. $\mathbf{C} = \mathbf{C}_{\text{stat}} + \mathbf{C}_{\text{sys}}$. The systematic uncertainties arise from the BEAMS method, which is applied to correct the bias generated by fits of both nuisance parameters from the light curve of SNe Ia and the cosmological parameters [57]. Therefore, \mathbf{C}_{sys} also accounts for the correlation among the apparent magnitudes of the Pantheon data set; i.e., the \mathbf{C}_{sys} is not a diagonal matrix: $(\mathbf{C}_{\text{sys}})_{i,j} \neq 0 \forall i, j$. For an ideal case, if we assume that uncertainties are uncorrelated the noise covariance matrix becomes diagonal, so the merit function comes to take a simple shape:

$$\chi_{\text{PaSNe}}^2(\theta) = \sum_{i=1}^{1048} \left(\frac{m_{\text{obs},i} - m_b(z_i; \theta)}{\sigma_{m_{\text{obs},i}}} \right)^2, \quad (48)$$

where the uncertainty of each measurement is the contribution of the statistical and systematic uncertainties; i.e., $\sigma_{m_{\text{obs},i}}^2 = \sigma_{m_{\text{stat},i}}^2 + \sigma_{m_{\text{sys},i}}^2$.

3. Remarks on the fitting and analysis strategies

We investigate the cosmological models associated with the mimetic field potentials, as outlined in section IV. The first family of models is characterized by an exponential potential $V(\phi) = V_0 e^{-\alpha \cdot \phi}$ (EP). We also consider a specific case with a fixed value of $\alpha = 1$, $V(\phi) = V_0 e^{-\phi}$, which is we label EPf. The second family considers an inverse quartic potential $V(\phi) = V_0 (1 + \delta \cdot \phi^2)^{-2}$ (IQP). In particular, the case $\delta = 1$ is identified as IQPf ($V(\phi) = V_0 (1 + \phi^2)^{-2}$). Table V provides a summary of the models, parameter space, and data sets employed for each fit. The numerical solutions in section IV indicate that for small values of α and δ , the curves closely resemble the Λ CDM model for early times, as expected. As a preliminary approximation, we consider $\alpha = 1$ and $\delta = 1$ to assess how well these models align with the data and analyze the differences compared to Λ CDM. In this case, the reduced parameter space also leads to a shorter computational time. However, it is acknowledged that for extended times periods, all curves will deviate from Λ CDM. Subsequently, we shall allow these parameters to be free, thus enabling a data-driven fitting process.

Since the MCMC performance requires of several iterations, the estimation of the all $H(z_i; \theta)$ and $m_b(z_i; \theta)$ models is computationally expensive. We therefore consider priors to expedite the characterization of the posterior distribution with the MCMC sampling approach. We consider two type of priors: *i*) uniform priors, $\mathcal{U}(a, b)$, that follow a top-hat function in the interval $[a, b]$, and *ii*) Gaussian priors, $\mathcal{N}(\bar{p}, \sigma_p)$, that follow a normal Gaussian distribution described by the mean and standard deviation of the p -parameter. The priors imposed on the free parameters are shown in Table V. For instance, the uniform priors over $\Omega_{\phi,0}$ and $\Omega_{k,0}$ guarantee the physical meaning of these densities. In other cases, the Gaussian and uniform priors are useful for alleviating the exploration of the parameter space. For example, we use the same constraint imposed in Ref. [55] for \mathcal{M} ; i.e., $\mathcal{P}(\mathcal{M}) = \mathcal{U}(23, 24)$.

Once the priors are established, we run the EMCEE with 50 chains and 14000 iteration steps to characterize the posterior distributions for each case. The first 3500 steps are excluded from each chain (the *burn-in* sample). Overall, the parameters from the cosmological modeling are computed from the marginalized the posterior distribution function, PDF(θ_i), over each parameter θ_i . Table VI presents the parameters and their uncertainties, i.e., respectively the median and uncertainty (the 16th and 84th percentiles) of its PDF(θ_i), for all cases studied.

To assess the goodness of fits we provide the chi-squared (χ^2) values in the parameter space recovered and the reduced chi-squared χ_{red}^2 values (accounting for the degrees of freedom). In addition, we can use criteria based on statistical information to determine whether the data favors one model over another. We selected two standard statistical indicators: 1) the Akaike Information Criterion [AIC, 58] and 2) the Bayesian Information Criterion [BIC, 59]. They are computed from the following expressions:

$$\text{AIC} = 2 N_\theta - 2 \ln(\mathcal{L}_{\text{max}}) \quad \text{and} \quad \text{BIC} = N_\theta \ln(n) - 2 \ln(\mathcal{L}_{\text{max}}), \quad (49)$$

where N_θ corresponds to the number of free parameters of the model, \mathcal{L}_{max} is the value of the likelihood function evaluated at the best fit, and n corresponds to the sample size. In the case of asymmetric distributions, where the median departs from the peak of the posterior, we use the latter to maintain the meaning of the definition of AIC and BIC. In our case, we have respectively $n_{\text{OHD}} = 51$ and $n_{\text{PaSNe}} = 1048$ for the OHD and Pantheon cases, which corresponds to $n_{\text{OHD+PaSNe}} = 1099$ for the joint analysis. These statistical quantities are confronted with those values obtained for the Λ CDM fits with curvature assumption cases, which are computed as:

$$\Delta \text{AIC}_{\text{model}} = \text{AIC}_{\text{model}} - \text{AIC}_{\Lambda\text{CDM}} \quad \text{and} \quad \Delta \text{BIC}_{\text{model}} = \text{BIC}_{\text{model}} - \text{BIC}_{\Lambda\text{CDM}}, \quad (50)$$

with “model” being the identification name of the model considered. $\Delta \text{AIC}_{\text{model}}$ and $\Delta \text{BIC}_{\text{model}}$ are computed with respect to fits that use the same database. The AIC, BIC, $\Delta \text{AIC}_{\text{model}}$ and $\Delta \text{BIC}_{\text{model}}$ are also listed in Table VI.

Model ID	Potential	Parameter space for non-flat models
EP	$V(\phi) = V_0 e^{-\alpha \cdot \phi}$	$\theta_{\text{OHD}} = \{H_0, \Omega_{\phi,0}, \Omega_{k,0}, \alpha\}$
		$\theta_{\text{PaSNe}} = \{H_0, \Omega_{\phi,0}, \Omega_{k,0}, \alpha, \mathcal{M}\}$
		$\theta_{\text{OHD+PaSNe}} = \{H_0, \Omega_{\phi,0}, \Omega_{k,0}, \alpha, \mathcal{M}\}$
EPf	$V(\phi) = V_0 e^{-\phi}$	$\theta_{\text{OHD}} = \{H_0, \Omega_{\phi,0}, \Omega_{k,0}\}$
		$\theta_{\text{PaSNe}} = \{H_0, \Omega_{\phi,0}, \Omega_{k,0}, \mathcal{M}\}$
		$\theta_{\text{OHD+PaSNe}} = \{H_0, \Omega_{\phi,0}, \Omega_{k,0}, \mathcal{M}\}$
IQP	$V(\phi) = V_0 (1 + \delta \cdot \phi^2)^{-2}$	$\theta_{\text{OHD}} = \{H_0, \Omega_{\phi,0}, \Omega_{k,0}, \delta\}$
		$\theta_{\text{PaSNe}} = \{H_0, \Omega_{\phi,0}, \Omega_{k,0}, \delta, \mathcal{M}\}$
		$\theta_{\text{OHD+PaSNe}} = \{H_0, \Omega_{\phi,0}, \Omega_{k,0}, \delta, \mathcal{M}\}$
IQPf	$V(\phi) = V_0 (1 + \phi^2)^{-2}$	$\theta_{\text{OHD}} = \{H_0, \Omega_{\phi,0}, \Omega_{k,0}\}$
		$\theta_{\text{PaSNe}} = \{H_0, \Omega_{\phi,0}, \Omega_{k,0}, \mathcal{M}\}$
		$\theta_{\text{OHD+PaSNe}} = \{H_0, \Omega_{\phi,0}, \Omega_{k,0}, \mathcal{M}\}$
Priors	$\mathcal{P}(H_0) : \mathcal{U}(0, 100)$ and $\mathcal{N}(73.24, 5)$ ($\text{km s}^{-1} \text{Mpc}^{-1}$)	
	$\mathcal{P}(\Omega_{\phi,0}) = \mathcal{U}(0, 1)$ and $\mathcal{N}(0.73, 0.05)$	
	$\mathcal{P}(\Omega_{k,0}) : \mathcal{U}(-0.2, 0.2)$, $\mathcal{P}(\alpha) = \mathcal{U}(-50, 50)$	
	$\mathcal{P}(\delta) = \mathcal{U}(-1000, \infty)$, and $\mathcal{P}(\mathcal{M}) = \mathcal{U}(23, 24)$	

TABLE V: Models, parameter spaces and priors considered in this study.

As a consistent test, the Λ CDM model for a flat universe is studied in order to compare the performance of our methodology with respect to analysis in the literature. We follow [52] and fit the three data sets to the Λ CDM model (assuming a flat universe) with the prior $\mathcal{P}(H_0) = \mathcal{N}(73.24, 1.74)$, where the parameter space consists of $\theta = \{\Omega_{\phi,0}, H_0\}$ for the OHD case, and $\theta = \{\Omega_{\phi,0}, H_0, \mathcal{M}\}$ for the PaSNe and OHD+PaSNe cases. For all analyses, the H_0 and $\Omega_{\phi,0}$ recovered are in full agreement with the results obtained by [52]. As an example, we obtained $H_0 = 70.51^{+0.85}_{-0.86} \text{ km s}^{-1} \text{Mpc}^{-1}$ and $\Omega_{\phi,0} = 0.265 \pm 0.013$ for the OHD+PaSNe case, while they reported $H_0 = 70.5 \pm 0.9 \text{ km s}^{-1} \text{Mpc}^{-1}$ and $\Omega_{\phi,0} = 0.265^{+0.013}_{-0.012}$ (see Table I in [52]). This confirms that our methodology is a reliable and robust approach.

B. Cosmological constraints

We provide the properties of non-flat cosmological models obtained with the three data sets (Table VI). We investigate the marginalized posteriors and corner plots (the 2D contours of the PDFs) for the Λ CDM (Fig. 11), EP (Figs. 12 and 13), and IQP (Figs. 14 and 15) cosmological models with spatial curvature. Overall, the non-flat cosmological models do not show substantial statistical preference over the base Λ CDM, EP, IQP models with the assumption of a flat universe, $\Omega_{k,0} = 0$. For example, the OHD+PaSNe analysis provides $\Omega_{k,0}$ values of $0.051^{+0.055}_{-0.054}$ (Λ CDM), $-0.020^{+0.117}_{-0.104}$ (EP), and $0.035^{+0.074}_{-0.069}$ (IQP) which are consistent with a flat universe. For reference, the results for the flat universe scenario are presented in appendix F (see Table VII).

We consider the OHD+PaSNe analysis as our reference model because it considers both data sets at the same time, which allow us to access more cosmological information. In spite of this, the goodness of fit appears to be better for the OHD cases, with χ^2_{red} around 0.55 for all models, tested (Table VI), although this low value also could reflect an underestimation of the uncertainties of the observational measurements are underestimated. In contrast, the OHD+PaSNe and PaSNe analysis respectively provide χ^2_{red} of 0.96 and ~ 0.98 . Close to unity. We therefore confirm that the performance of the fits is robust and similar when the same data set is considered.

Regarding the curved universe scenarios, the $\Omega_{k,0}$ values are compatible with zero for all the cases studied, with the significance of detection being around one (see Table VI). Overall, the OHD and OHD+PaSNe analysis prefer positive curvature in contrast to the PaSNe fits. Only the IQP modeling shows positive curvature values for the three data sets. The non-flat Λ CDM scenario yields $\Omega_{k,0}$ values of 0.047 ± 0.058 , $-0.047^{+0.077}_{-0.075}$, and $0.051^{+0.055}_{-0.054}$ for the OHD, PaSNe and OHD+PaSNe fits, respectively. Despite our higher uncertainties, these values are compatible

Dataset	$\Omega_{\phi,0}$	α	δ	$\Omega_{k,0}$	H_0	\mathcal{M}	χ^2_{\min}	χ^2_{red}	AIC	BIC	ΔAIC	ΔBIC
ΛCDM												
OHD	0.707 ± 0.045	—	—	0.047 ± 0.058	$70.23^{+1.26}_{-1.21}$	—	26.5	0.55	32.5	38.3	—	—
PaSNe	$0.730^{+0.043}_{-0.045}$	—	—	$-0.047^{+0.077}_{-0.075}$	$73.41^{+4.89}_{-5.04}$	23.81 ± 0.01	1027.2	0.98	1035.2	1055.0	—	—
OHD+PaSNe	0.691 ± 0.039	—	—	$0.051^{+0.055}_{-0.054}$	$69.39^{+1.00}_{-0.98}$	23.80 ± 0.01	1055.0	0.96	1063.0	1083.0	—	—
EP												
OHD	0.715 ± 0.042	$-11.94^{+34.53}_{-25.31}$	—	$0.082^{+0.078}_{-0.129}$	$70.34^{+1.35}_{-1.29}$	—	26.4	0.56	34.4	42.1	1.9	3.8
PaSNe	$0.727^{+0.041}_{-0.042}$	$-2.54^{+32.09}_{-31.21}$	—	$-0.041^{+0.099}_{-0.093}$	$73.35^{+4.88}_{-5.06}$	23.81 ± 0.01	1026.9	0.98	1036.9	1061.7	1.7	6.7
OHD+PaSNe	$0.699^{+0.037}_{-0.038}$	$18.08^{+19.00}_{-27.50}$	—	$-0.020^{+0.117}_{-0.104}$	$69.49^{+1.01}_{-0.99}$	23.81 ± 0.01	1055.0	0.96	1065.0	1090.0	2.0	7.0
EPf												
OHD	$0.706^{+0.045}_{-0.044}$	—	—	0.045 ± 0.058	$70.20^{+1.24}_{-1.21}$	—	26.5	0.55	32.5	38.3	0	0
PaSNe	$0.730^{+0.043}_{-0.044}$	—	—	$-0.051^{+0.077}_{-0.072}$	$73.29^{+4.88}_{-5.01}$	23.81 ± 0.01	1027.0	0.98	1035.0	1054.8	-0.2	-0.2
OHD+PaSNe	0.692 ± 0.039	—	—	$0.047^{+0.054}_{-0.055}$	$69.41^{+1.01}_{-0.98}$	23.80 ± 0.01	1054.9	0.96	1062.9	1082.9	-0.1	-0.1
IQP												
OHD	$0.717^{+0.042}_{-0.043}$	—	$1568.9^{+2644.8}_{-1859.9}$	$0.116^{+0.061}_{-0.095}$	$71.03^{+1.65}_{-1.53}$	—	29.1	0.62	37.1	44.8	4.6	6.5
PaSNe	$0.725^{+0.042}_{-0.041}$	—	$7012.1^{+10114.6}_{-5753.0}$	$0.063^{+0.092}_{-0.110}$	$73.88^{+4.89}_{-4.95}$	23.80 ± 0.01	1027.8	0.99	1037.8	1062.6	2.6	7.6
OHD+PaSNe	0.696 ± 0.041	—	$-368.8^{+970.0}_{-469.5}$	$0.035^{+0.074}_{-0.069}$	$69.41^{+1.00}_{-0.97}$	23.80 ± 0.01	1054.5	0.96	1064.5	1089.5	1.5	6.5
IQPf												
OHD	0.707 ± 0.045	—	—	$0.048^{+0.058}_{-0.057}$	$70.23^{+1.27}_{-1.22}$	—	26.5	0.55	32.5	38.3	0	0
PaSNe	$0.730^{+0.043}_{-0.044}$	—	—	$-0.048^{+0.077}_{-0.074}$	$73.27^{+5.01}_{-4.98}$	23.81 ± 0.01	1027.1	0.98	1035.1	1054.9	-0.1	-0.1
OHD+PaSNe	0.692 ± 0.039	—	—	0.050 ± 0.054	$69.41^{+1.00}_{-0.99}$	23.80 ± 0.01	1054.9	0.96	1062.9	1082.9	-0.1	-0.1

TABLE VI: Parameters and uncertainties obtained for the non-flat cosmological models investigated. The identification names and field potentials for the Λ CDM model and mimetic gravity models (EP, EPf, IQP and IQPf) are listed in Table V. The properties of these non-flat cosmological models are obtained using three data set: the observational Hubble database from the cosmic chronometers (OHD), the Pantheon database for Type Ia supernovae (PaSNe), and the simultaneous analysis of the OHD and PaSNe data sets (OHD+PaSNe). The statistical parameters ΔAIC and ΔBIC are computed with respect to the non-flat Λ CDM results for the same database.

with the literature [for example, see 42, 43, 60–67]. For instance, [60] obtained $\Omega_{k,0}$ between -0.043 up to 0.0008 using the CMB temperature and polarization power spectra (TT, TE and EE), BAO, and the Pantheon sample for the base Λ CDM with spatial curvature. The CMB data alone have provided significance between 2 up to 3σ that depart from the $\Omega_{k,0} = 0$ scenario [42, 43, 64, and references therein]; for example, $\Omega_{k,0} = -0.044^{+0.018}_{-0.019}$ was obtained from the *Planck* data [65]. Although the new analysis of the *Planck* data have allowed stronger constraints such as $-0.025^{+0.013}_{-0.010}$ [66] and -0.012 ± 0.010 [67] to be achieved. Including the CMB data is beyond the scope of this paper, although this is one of the goals of a future paper.

For the PaSNe fits, we also observe that negative values of $\Omega_{k,0}$ are associated with high values of the H_0 ($\sim 73.4 \text{ km s}^{-1} \text{ Mpc}^{-1}$) and $\Omega_{\phi,0}$ (~ 0.73) parameters, except for the EPf model where $\Omega_{k,0} > 0$. The correlation between them is not clear in the corner plots (see the blue 2D-PDFs of $\Omega_{k,0}$ versus H_0 and $\Omega_{\phi,0}$). However, the OHD+PaSNe analysis show an anti-correlation between $\Omega_{k,0}$ and H_0 . This is in the opposite direction when the CMB data is considered, which provides higher values of $\Omega_{k,0}$ as H_0 increases; see, for example, [4, 66, 67] for only the CMB data. Previous studies have also reported higher values of H_0 when only the Type Ia supernovae data are considered [e.g., 52, 68–70]. For instance, [52] obtained values of H_0 of 73.2 ± 1.7 and $70.5 \pm 0.9 \text{ km s}^{-1} \text{ Mpc}^{-1}$ respectively for their SNeIa and Joint (similar to our PSNe and OHD+PSNe) fits for the Λ CDM model. They also reported this trend for their four models [see Table I in 52]. For non-flat Universes, for example, [60], considering the CMB+BAO and CMB+PaSNe+BAO for all model investigated, observed lower values of H_0 for the CMB+PaSNe data set with respect to fits where the CMB+PaSNe cases always provided $\Omega_k < 0$. This change in trend could be connected with the inclusion of the CMB data (temperature and polarization power spectra).

Regarding the possibility of alleviating the H_0 tension, this work has not compared the model to Λ CDM in much detail for intermediate and early times, and this comparison will likely depend on the specific potential in most cases.

On the other hand, there does not appear to be a reduction in H_0 that can be attributed to the model itself rather than to the data. In all cases, the values obtained are lower in the combined data, followed by the *OHD* values, which are lower than those reported in [71]. In any case, to gain certainty, the model should be compared with CMB measurements, such as those reported in [65].

That said, it is not possible to make a comparison, since no comparison was made at intermediate redshifts, as

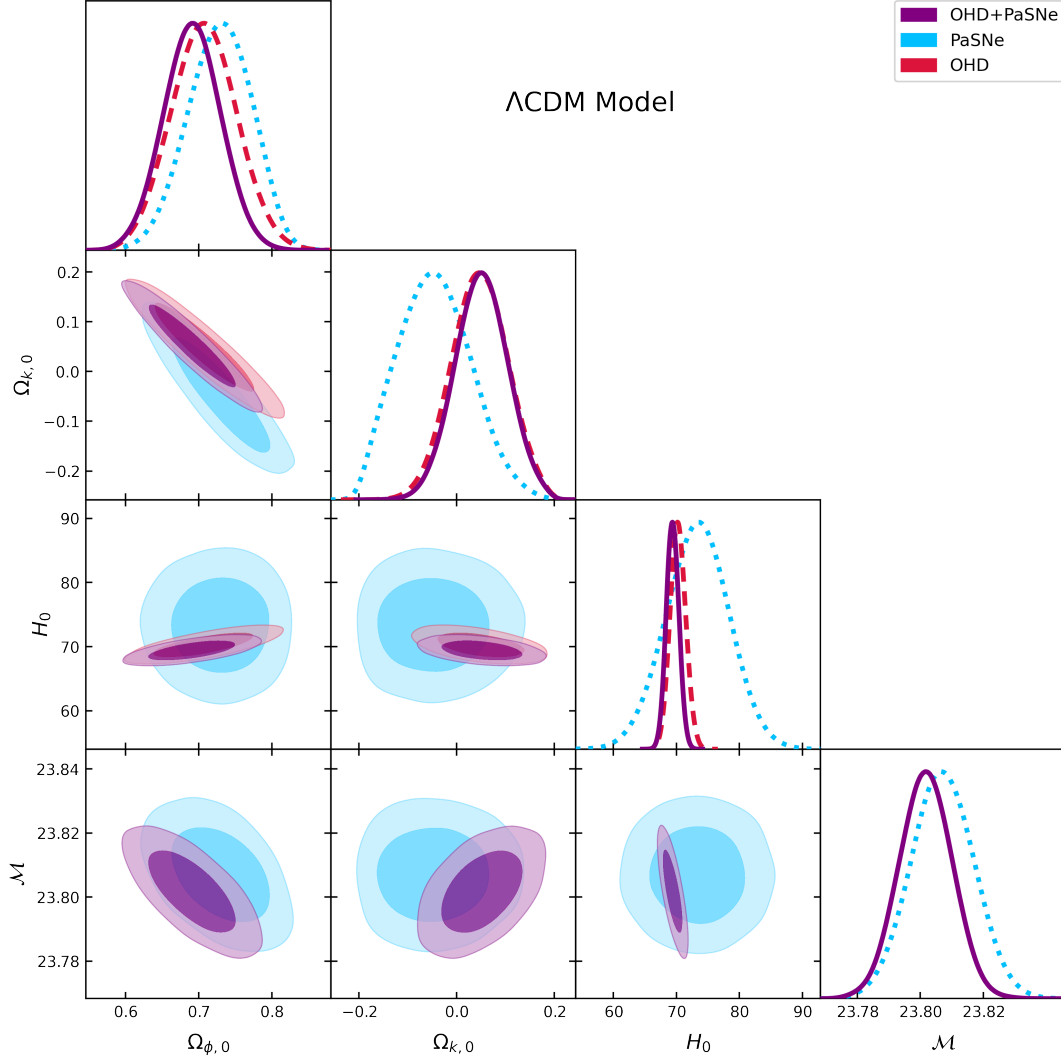


FIG. 11: Marginalized posteriors and correlation plots for the parameters $\Omega_{\phi,0}$, $\Omega_{k,0}$, H_0 , \mathcal{M} that describe the non-flat Λ CDM model. The contours represent the 68.3% and 95.4% confidence levels. The results obtained from the OHD+PaSNe, PaSNe, and OHD analysis (Table VI) are identified respectively by the purple, blue, and red colors. H_0 is in units of $\text{km s}^{-1} \text{Mpc}^{-1}$, while $\Omega_{\phi,0}$, $\Omega_{k,0}$, and \mathcal{M} are dimensionless units.

done in [72], and it was not evaluated for CMB measurements either. All of this could constitute future research.

1. Non-flat Exponential Potential models

Regarding the EP model, the $\Omega_{\phi,0}$, H_0 , and \mathcal{M} values recovered are in agreement with those obtained for the non-flat Λ CDM analyses (for all cases). These are performed with very similar goodness of fit (see Table VI), producing $\chi^2 = 0.96$ for both the non-flat Λ CDM and the EP models (OHD+PaSNe case), although we obtained a relatively high $\Delta\text{BIC} = 7$ and moderate $\Delta\text{AIC} = 2$, which favor the non-flat Λ CDM over the EP models. The OHD+PaSNe analysis produces $\Omega_{k,0} = -0.02^{+0.12}_{-0.104}$, which contrasts with the positive curvature from the non-flat Λ CDM model ($\Omega_{k,0}^{\Lambda\text{CDM}} = 0.051^{+0.055}_{-0.054}$), although still consistent and compatible with zero at one- σ . In addition, we observed that asymmetric PDFs for $\Omega_{k,0}$ and their behaviors depend on the data used. The marginalized PDFs reach their maximum at around -0.01 (OHD+PaSNe and PaSNe) and 0.013 (OHD), respectively. We also found that α is described by asymmetric marginalized PDFs, and that the high dispersion does not allow good constraints on α . For the OHD+PaSNe and OHD cases, their PDFs are peaking at around 25 and -30 , respectively. In contrast, the PDF

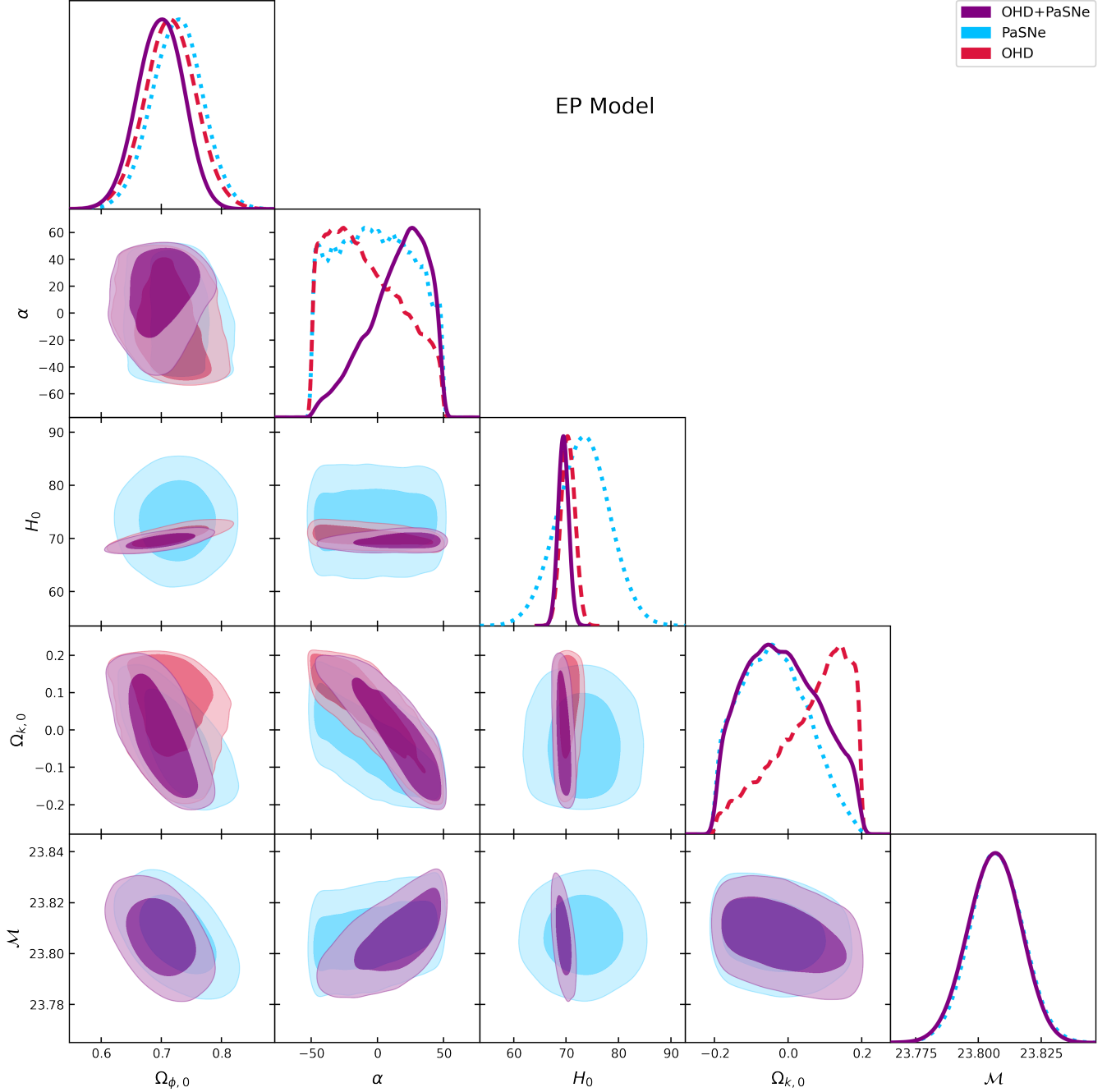


FIG. 12: Marginalized posteriors and correlation plots for the parameters $\Omega_{\phi,0}$, α , $\Omega_{k,0}$, H_0 , \mathcal{M} that describe the EP model (the exponential potential) with spatial curvature. The contours represent the 68.3% and 95.4% confidence levels. The results obtained from the OHD+PaSNe, PaSNe and OHD analysis, Table VI, are identified respectively by the purple, blue and red colors. H_0 is in units of $\text{km s}^{-1} \text{Mpc}^{-1}$, while $\Omega_{\phi,0}$, α , $\Omega_{k,0}$, and \mathcal{M} are dimensionless units.

of α is poorly characterized for the PaSNe data, yielding $\alpha = 3 \pm 32$. We therefore obtained a wide range of values of α that follow the imposed uniform prior ranging from -50 to 50 , with $\alpha = 18^{+19}_{-28}$ (OHD+PaSNe) being the most restrictive value. This is a poor constraint on α , which can increase the degeneracy between other parameters of the EP model.

The contour plot between α and $\Omega_{k,0}$ shows an anti-correlation (see Fig. 12), where the extended tails are slightly shifted to negative and positive values of $\Omega_{k,0}$ and α , respectively. For other 2D contours, we observed no significant

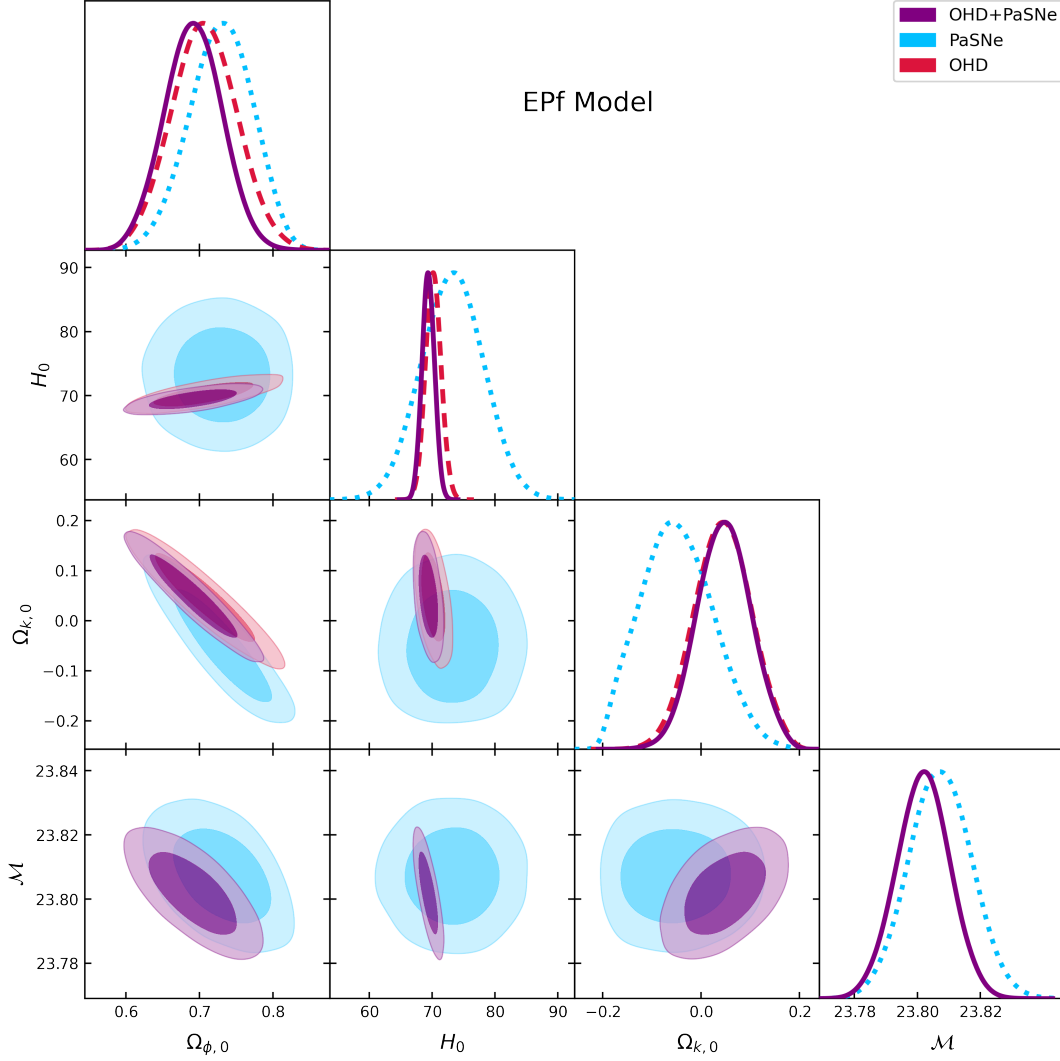


FIG. 13: Marginalized posteriors and correlation plots for the parameters $\Omega_{\phi,0}$, α , $\Omega_{k,0}$, H_0 , \mathcal{M} that describe the EPf model (the exponential potential with $\alpha = 1$) with spatial curvature. The contours represent the 68.3% and 95.4% confidence levels. The results obtained from the OHD+PaSNe, PaSNe and OHD analysis, Table VI, are identified respectively by the purple, blue and red colors. H_0 is in units of $\text{km s}^{-1} \text{Mpc}^{-1}$, while $\Omega_{\phi,0}$, α , $\Omega_{k,0}$ and \mathcal{M} are dimensionless units.

change with respect to the non-flat Λ CDM. For instance, the $\Omega_{\phi,0} - \Omega_{k,0}$ PDFs appear to be broader than the non-flat Λ CDM cases. This suggests that the $\alpha - \Omega_{k,0}$ anti-correlation could be independent of other parameters, although we must keep in mind that α is poorly characterized.

To avoid the effects of considering α as a free parameter, we explored the EP model with $\alpha = 1$ (called EPf, Fig. 13). This case provides results more consistent with the Λ CDM than with those from the EP model. For instance, the OHD+PaSNe case is performed with $\chi^2_{\text{red}} = 0.96$ for both the non-flat Λ CDM and the EPf models, with $\Delta\text{AIC} = -0.1$ and $\Delta\text{BIC} = -0.1$, which, on a negligible level, favor the EPf results. We recover a positive-curvature $\Omega_{k,0} = 0.047^{+0.054}_{-0.055}$, $H_0 = 69.4 \pm 1.0 \text{ km s}^{-1} \text{Mpc}^{-1}$, and $\Omega_{\phi,0} = 0.692 \pm 0.039$. In addition, the EPf model prefers positive $\Omega_{k,0}$ at 0.8σ , in contrast to the negative curvature at 1.7σ from the EP model which is slightly more shifted towards $\Omega_{k,0} = 0$. Moreover, the marginalized PDFs of $\Omega_{k,0}$ are symmetrical and become more sharpened than in the cases of the EP analysis. These two features are also extended to the behavior of the 2D contours for $\Omega_{\phi,0} - \Omega_{k,0}$, which now are more compatible with the corner plots from the non-flat Λ CDM analysis.

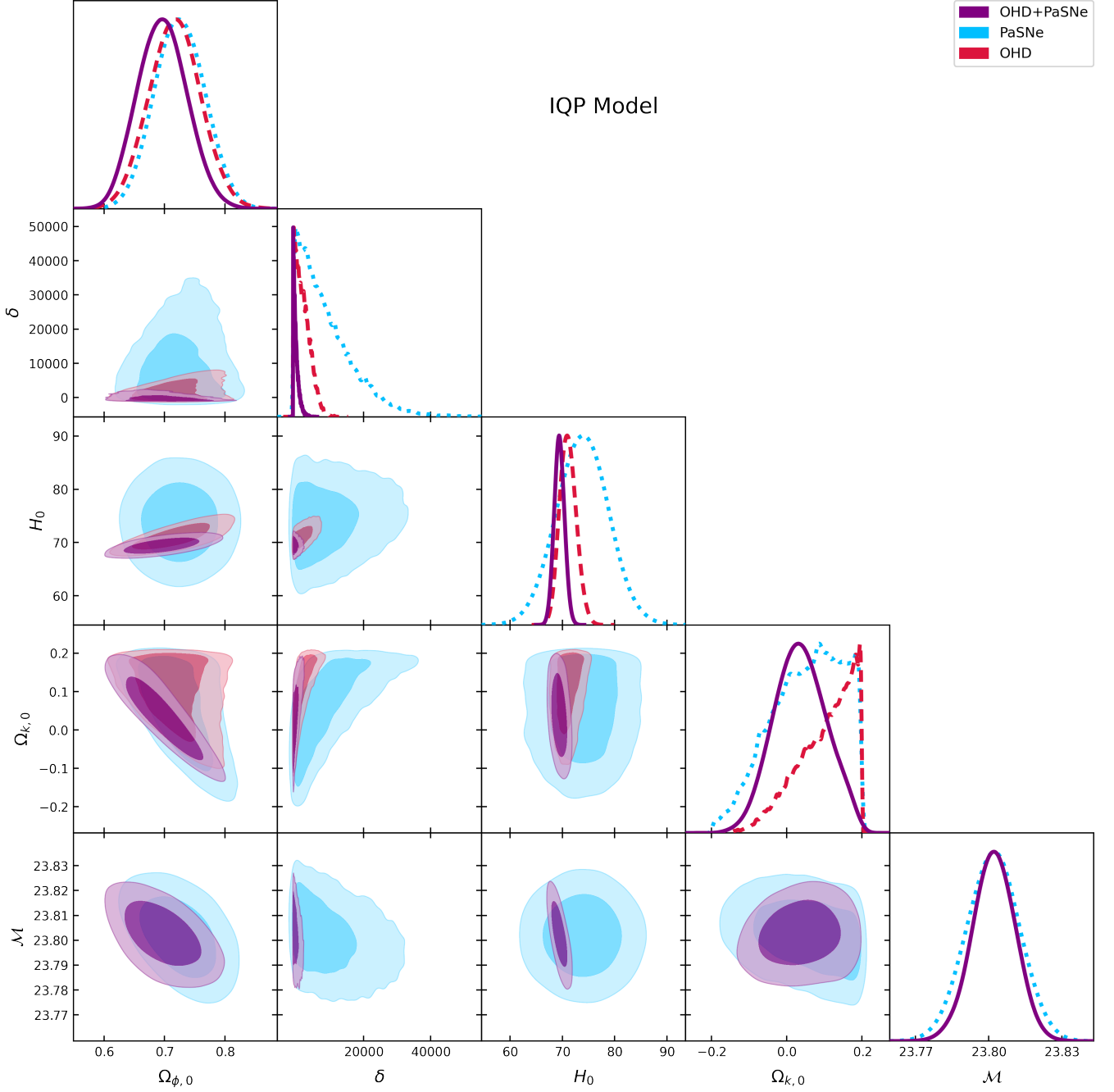


FIG. 14: Marginalized posteriors and correlation plots for the parameters $\Omega_{\phi,0}$, δ , $\Omega_{k,0}$, H_0 , \mathcal{M} that describe the IQP model (the inverse quadratic potential) with spatial curvature. The contours represent the 68.3% and 95.4% confidence levels. The results obtained from the OHD+PaSNe, PaSNe and OHD analysis, Table VI, are respectively identified by the purple, blue and red colors. H_0 is in units of $\text{km s}^{-1} \text{Mpc}^{-1}$, while $\Omega_{\phi,0}$, δ , $\Omega_{k,0}$ and \mathcal{M} are dimensionless units.

2. Non-flat Inverse Quartic Potential models

As for the EP model, the parameters ($\Omega_{\phi,0}$, H_0 and \mathcal{M}) and the goodness of the fits obtained from the IQP models agree with the results from the non-flat ΛCDM analyses (see Fig. 14). For the OHD+PaSNe, the $\chi^2 = 0.96$ is the same for both non-flat ΛCDM and IQP models, yielding $\Omega_{k,0} = 0.035^{+0.074}_{-0.069}$, $H_0 = 69.4 \pm 1.0 \text{ km s}^{-1} \text{Mpc}^{-1}$, and $\Omega_{\phi,0} = 0.696 \pm 0.041$. The positive curvature moves slightly (with respect to the non-flat ΛCDM model) towards

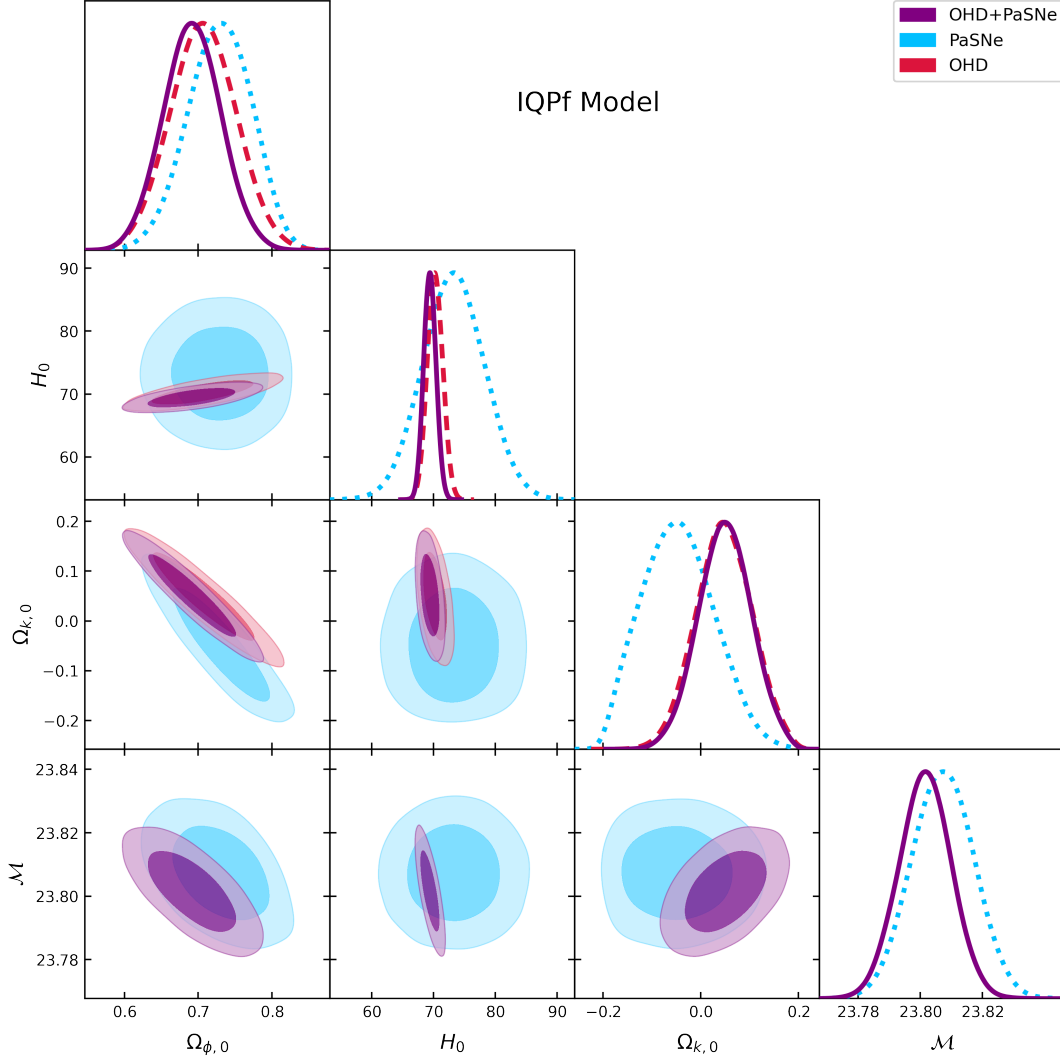


FIG. 15: Marginalized posteriors and correlation plots for the parameters $\Omega_{\phi,0}$, $\Omega_{k,0}$, H_0 , \mathcal{M} that describe the IQPf model (the inverse quadratic potential with $\delta = 1$) with spatial curvature. The contours represent the 68.3% and 95.4% confidence levels. The results obtained from the OHD+PaSNe, PaSNe and OHD analysis, Table VI, are respectively identified by the purple, blue and red colors. H_0 is in units of $\text{km s}^{-1} \text{Mpc}^{-1}$, while $\Omega_{\phi,0}$, $\Omega_{k,0}$ and \mathcal{M} are dimensionless units.

$\Omega_{k,0} = 0$ at a level of 0.5σ , although the uncertainty is broader in the IQP model. In addition, the $\Delta\text{BIC} = 6.6$ and moderate $\Delta\text{AIC} = 1.5$ favor the non-flat ΛCDM over the IQP models with freely sampled δ .

The marginalized PDFs of δ are asymmetrical, particularly for the OHD and PaSNe cases, with tails extending up to unreasonable values of 40000 in the worst case. We can therefore provide only a weak description of the δ . The sharper PDF results from the OHD+PaSNe case, even though its peak is located near the lower bound of the uniform prior imposed on δ . The OHD and PaSNe analysis also show a significant impact on the shape of the $\Omega_{k,0}$ PDFs, mainly owing to the irregular description of the δ parameter. For the OHD analysis, the peak of the PDF reaches the upper bound of the uniform prior imposed on $\Omega_{k,0}$, while the curve is wider for the PaSNe case, peaking around 0.1. We need a more restrictive prior to evaluate possible correlation between δ and other parameters such as $\Omega_{k,0}$ (as for the EP analysis).

For the case with $\delta = 1$ (IQPf), we obtained a parameter space in full agreement with the non-flat ΛCDM results, where the goodness of fit and comparison parameters (ΔBIC and ΔAIC) are practically equal for each database that explores both models (Table VI). For example, the OHD+PaSNe case is performed with $\chi^2_{\text{red}} = 0.96$ for both non-flat ΛCDM and IQPf models, with $\Delta\text{AIC} = -0.1$ and $\Delta\text{BIC} = -0.1$ favoring (to a negligible degree) the IQPf results. The IQPf analysis provide sharper and more symmetrical PDF behavior than the IQP model analysis (see

Fig. 15). The correlation plots are also now well delimited (with respect to the IQP models). The PDFs of $\Omega_{k,0}$ are described within the range of the uniform prior considered for $\Omega_{k,0}$. In particular, the OHD and PaSNe curves do not reach the prior upper limits as their maximum. For example, in the OHD case, the peak is now at $\Omega_{k,0} \approx 0.48$ in contrasted to the value of -0.2 from the IQP model. For the OHD+PaSNe analysis, we obtained $\Omega_{k,0} = 0.050 \pm 0.054$, $H_0 = 69.4 \pm 1.0 \text{ km s}^{-1} \text{ Mpc}^{-1}$ and $\Omega_{\phi,0} = 0.692 \pm 0.039$, which is compatible with the non-flat Λ CDM results and with a flat universe.

VI. CONCLUSIONS

We presented a dynamic description of isotropic and homogeneous Friedmann-Lemaître-Robertson-Walker cosmological models, with positive spatial curvature within the framework of mimetic gravity theory. We consider families of specific mimetic field potentials: the exponential potential (EP), the inverse square potential (ISP), and the inverse quartic potential (IQP). In addition, the parameters of the EP and IQP models were fitted with observational data from the Pantheon Type Ia Supernovae database and the Observational Hubble database from cosmic chronometers.

First, we considered a generic potential for the mimetic field and determined the critical points of the dynamical system. We analyzed the stability of each of them using linear stability and the centre manifold method for cases with null eigenvalues of the variation matrix. To understand the dynamics of the system at infinity, we studied the global phase space of the dynamical system by projecting on the Poincaré sphere. The dynamical system is four-dimensional, with the exception of the ISP ($V(\phi) \propto 1/\phi^2$) for which the dimension reduces to three. We explored the dynamics on invariant submanifolds and revealed trajectories that can evolve to a de Sitter universe and a division of the phase space in contracting and expanding epochs.

For the ISP ($V = \gamma/\phi^2$), the dynamical system reduced to a three-dimensional autonomous system. Trajectories starting from the matter-dominated critical line could evolve towards a future attractor representing a solution dominated by dark matter and dark energy, exhibiting acceleration under certain conditions. Additionally, we identified trajectories that can enter the contracting phase space and recollapse to a big crunch. The phase space of this potential does not include the solution representing Einstein static universe. For the EP ($V = V_0 e^{-\alpha\phi}$), however, we found that one equation decouples from the others, resulting in a three dimensional reduced dynamical system. The dynamical evolution of the system depends on the sign of α . The invariant submanifold $\zeta = 0$ divides the phase space into two regions, such that trajectories with different signs of α only have dynamics in their respective regions, $\alpha < 0$ ($\alpha > 0$) associated with the region $\zeta < 0$ ($\zeta > 0$). When $\alpha = 0$, the trajectories are confined to the invariant submanifold $\zeta = 0$. We mainly found trajectories with $\alpha < 0$ that are past asymptotic to the matter-dominated critical line, evolving towards a point corresponding to an expanding de Sitter accelerated solution dominated by the mimetic field $\Omega_\phi = 1$. We also observed trajectories with $\alpha > 0$ that are past asymptotic to the matter-dominated critical line, approximating the point dominated by the mimetic field, but then evolving to a point at infinity, and then going to another point, also at infinity. We also found trajectories that are both past asymptotic and future asymptotic to the Einstein static solution, as well as trajectories starting from the matter-dominated critical line that, after some expansion, begin to contract and collapse to a big crunch. Therefore, by applying dynamical system techniques we found that cosmological models in mimetic gravity can support physically relevant solutions representing different stages of cosmic evolution.

Utilizing data from the Observational Hubble Dataset (OHD) and the Pantheon database of Type Ia Supernovae (PaSNe), observational constraints on the parameters of non-flat cosmological models (EP and IQP models) were obtained through Bayesian statistical analysis. In all cases, the $\Omega_{k,0}$ values are consistent with a flat Universe. In fact, the parameter space of non-flat models are in agreement with the parameter space obtained for models assuming flat curvature. For non-flat curvature cases, both the EP and IQP analyses produce results in agreement with the non-flat Λ CDM model. The current data provide weak constraints on the main parameters describing the EP and IQP models. For the EP model and the OHD+PaSNe case, we find $\alpha = 18_{-28}^{+19}$, which shows an anticorrelation with $\Omega_{k,0}$. For the IQP model, $\beta = -369_{-470}^{+970}$ is a weak constraint (the OHD+PaSNe case). Despite the provided observational constraints, the viability of mimetic gravity models is supported by the data sets, and these models can effectively describe the late-time accelerated expansion of the universe. Comparison with the Λ CDM model using the AIC and BIC statistical indicators provided insights into the observational support of the models. In this context, the CMB data could improve our current constraints on the EP and IQP models.

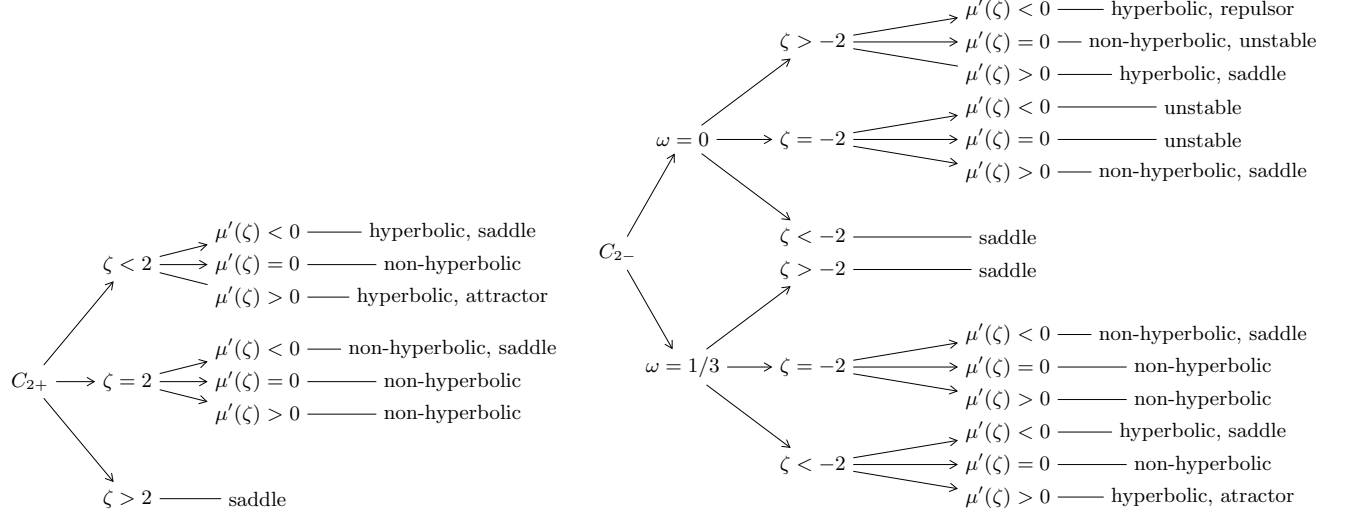
Acknowledgments

We thank Terry Mahoney (Scientific Editorial Service of the IAC) for proofreading this manuscript. This work is partially supported by ANID Chile through FONDECYT Grants N° 1201673 (A.F. and J.C.H.) and N° 1220871 (A. F.

and Y. V.). Y.V. acknowledges the financial support of DIDULS/ULS, through the project PTE2121313. This work is also funded by ANID–Millennium Program–ICN2019.044 (Chile). The authors wish to thank the FIULS 2030 project 18ENI2-104235 – CORFO for providing computing resources. CHLC acknowledges financial support by the Spanish Ministry of Science and Innovation under the projects AYA2017-84185-P and PID2020-120514GB-I00, and the ACIISI, Consejería de Economía, Conocimiento y Empleo del Gobierno de Canarias and the European Regional Development Fund (ERDF) under grant with reference ProID2020010108.

Appendix A: Dynamical character of points C_{2+} and C_{2-}

In this appendix we show the dynamical character of the critical points C_{2+} and C_{2-} for the different values of ζ and $\mu'(\zeta)$.



Appendix B: Centre manifold method

In this appendix we describe the centre manifold method for analyzing the stability of critical points that cannot be categorized as hyperbolic stable or unstable owing to the presence of null eigenvalues in the variation matrix. We illustrate the method by specifically focusing on the critical point B_+ for $\omega = 0$, $(\zeta^2 \mu(\zeta))|_{\zeta=0}$ and $\frac{d}{d\zeta}(\zeta^2 \mu(\zeta))|_{\zeta=0}$. To enhance the clarity and conciseness in our expressions, we define $M(\zeta) = -\sqrt{3}\zeta^2 \mu(\zeta)$.

The critical point B_+ with coordinates $(1, 0, 1, 0)$ can be shifted to the origin by applying the transformation $Q \rightarrow Q + 1$ and $\beta \rightarrow \beta + 1$. After this transformation, the critical point is located at the origin and the Jacobian matrix reads

$$J_{B_+} = \begin{pmatrix} -2 & 0 & 0 & 0 \\ 0 & -3 & 0 & \sqrt{3} \\ 0 & 0 & -3 & -\frac{\sqrt{3}}{2} \\ 0 & 0 & 0 & 0 \end{pmatrix}. \quad (B1)$$

Now, diagonalizing the Jacobian matrix with the matrix of eigenvectors, given by

$$S = \begin{pmatrix} 1 & 0 & 0 & 0 \\ 0 & 1 & 0 & 1 \\ 0 & 0 & 1 & -\frac{1}{2} \\ 0 & 0 & 0 & \sqrt{3} \end{pmatrix}, \quad (B2)$$

and introducing the new set of variables

$$\begin{pmatrix} y_1 \\ y_2 \\ y_3 \\ x \end{pmatrix} = S^{-1} \begin{pmatrix} Q \\ \tilde{\Omega}_\lambda \\ \beta \\ \zeta \end{pmatrix}, \quad (\text{B3})$$

the system of equations transforms to

$$x' = Ax + f(x, \mathbf{y}) \quad (\text{B4})$$

$$\mathbf{y}' = \mathbf{B}\mathbf{y} + \mathbf{g}(x, \mathbf{y}) \quad (\text{B5})$$

where

$$\mathbf{y} = \begin{pmatrix} y_1 \\ y_2 \\ y_3 \end{pmatrix}, \quad A = 0, \quad \mathbf{B} = \begin{pmatrix} -2 & 0 & 0 \\ 0 & -3 & 0 \\ 0 & 0 & -3 \end{pmatrix}, \quad \mathbf{g} = \begin{pmatrix} g_1 \\ g_2 \\ g_3 \end{pmatrix}, \quad (\text{B6})$$

and f, \mathbf{g} are nonlinear functions of the coordinates x and \mathbf{y} . For brevity, we omit explicit expressions for f and \mathbf{g} .

The center manifold for (B4) can be locally represented as

$$\{(x, \mathbf{y}) | \mathbf{y} = \mathbf{h}(x), \mathbf{h}(0) = 0, \nabla \mathbf{h}(0) = 0\}, \quad (\text{B7})$$

where $\mathbf{h}(x) = \begin{pmatrix} h_1(x) \\ h_2(x) \\ h_3(x) \end{pmatrix}$ satisfies the following quasilinear differential equation

$$\nabla \mathbf{h}(x)(Ax + f(x, \mathbf{h}(x))) - \mathbf{B}\mathbf{h}(x) - \mathbf{g}(x, \mathbf{h}(x)) = 0. \quad (\text{B8})$$

For the purpose of stability, a series expansion of $\mathbf{h}(x)$ is considered, where

$$h_i(x) = a_i x^2 + b_i x^3 + \mathcal{O}(x^4) \text{ for } i = 1, 2, 3. \quad (\text{B9})$$

Additionally, the function $M(x)$ is assumed to have a Taylor series expansion around $x = 0$, with $M(0) = 0$ and $M'(0) = 0$. By inserting these expressions into Eq. (B8), the coefficients a_i and b_i can be obtained. Consequently, the dynamics of the system reduced to the centre manifold is given by

$$u' = Au + f(u, \mathbf{h}(u)). \quad (\text{B10})$$

Upon inserting the functions h_i , the expression becomes

$$u' = \frac{M''(0)}{2\sqrt{3}}x^2 + \left(-\frac{M''(0)}{4\sqrt{3}} + \frac{M^{(3)}(0)}{6\sqrt{3}}\right)x^3 + \mathcal{O}(x^4). \quad (\text{B11})$$

Appendix C: Poincaré projection method

In this appendix we review the Poincaré projection method that we used to analyze the critical points at infinity. Here, we apply the method for a general three-dimensional dynamical system; however, it can be straightforwardly generalized to higher-dimensional system.

Consider the following autonomous dynamical system described by the set of equations

$$\dot{x} = P(x, y, w), \quad \dot{y} = Q(x, y, w), \quad \dot{w} = R(x, y, w). \quad (\text{C1})$$

We assume that the variable w is compact, and that P, Q and R are polynomials functions of x, y and w . Our interest is to describe the behavior of the system at infinity, $x \rightarrow \infty$ and/or $y \rightarrow \infty$. Also, we consider P and Q

polynomials of maximum degree m of the non-compact variables x and y , whereas R is a polynomial of maximum degree $m - 1$ of the non-compact variables, this is the case of section III C 1 with $m = 3$. Then, compactifying the phase space by means of the following change of variable

$$X = \frac{x}{\sqrt{1+x^2+y^2}}, \quad Y = \frac{y}{\sqrt{1+x^2+y^2}}, \quad Z = \frac{1}{\sqrt{1+x^2+y^2}}, \quad (\text{C2})$$

we obtain

$$\begin{aligned} \dot{X} &= Z((1-X^2)P - XYQ), \\ \dot{Y} &= Z(-XYP + (1-Y^2)Q), \\ \dot{Z} &= -Z^2(XP + YQ). \end{aligned} \quad (\text{C3})$$

Now, the behavior near $Z = 0$ is given by:

$$\begin{aligned} P(x, y, w) &= P\left(\frac{X}{Z}, \frac{Y}{Z}, w\right) \sim Z^{-m}, \\ Q(x, y, w) &= Q\left(\frac{X}{Z}, \frac{Y}{Z}, w\right) \sim Z^{-m}, \\ R(x, y, w) &= R\left(\frac{X}{Z}, \frac{Y}{Z}, w\right) \sim Z^{-m+1}. \end{aligned} \quad (\text{C4})$$

Defining $P^* = Z^m P$, $Q^* = Z^m Q$ and $R^* = Z^{m-1} R$, performing the change of variable $d\tau = Z^{1-m} dt$, and setting $Z = 0$, we then arrive at

$$\begin{aligned} X' &= -Y(XQ^* - YP^*), \\ Y' &= X(XQ^* - YP^*), \\ w' &= R^*. \end{aligned} \quad (\text{C5})$$

Appendix D: Stability at infinity

In this appendix we show a way of analyzing the stability at infinity using a second projection of any point in the space described by the Poincaré projection to a plane tangential to it, in this way avoiding the divergences of the eigenvalues. First of all, it should be said that it is necessary for some free axes to coincide locally in direction and sign with the projection, so the signs are adjusted manually. Below, without loss of generality, we consider a 2-dimensional example to understand this concept. This is easily extensible to more dimensions. Consider the following autonomous dynamical system described by the set of equations:

$$\dot{x} = P(x, y), \quad \dot{y} = Q(x, y). \quad (\text{D1})$$

We can then compactify the phase space, as explained in the previous appendix, by using the following change of variables:

$$X = \frac{x}{\sqrt{1+x^2+y^2}}, \quad Y = \frac{y}{\sqrt{1+x^2+y^2}}, \quad Z = \frac{1}{\sqrt{1+x^2+y^2}}. \quad (\text{D2})$$

Now suppose we want to analyze critical points for $X < 1$. We choose $X < 1$ to note the choice of sign, therefore:

$$\xi = -\frac{Y}{X} = -\frac{y}{x}, \quad \zeta = -\frac{Z}{X} = -\frac{1}{x}. \quad (\text{D3})$$

Suppose that the order of the largest homogeneous polynomial for $P(x, y)$ and $Q(x, y)$ in x, y is m . By performing a change in the time coordinate such that $dt = \zeta^{m-1} d\tau$, the resulting system will then be:

$$\xi' = \zeta^m \left(Q\left(\frac{-1}{\zeta}, \frac{\xi}{\zeta}\right) + \xi P\left(\frac{-1}{\zeta}, \frac{\xi}{\zeta}\right) \right), \quad \zeta' = \zeta^{m+1} P\left(\frac{-1}{\zeta}, \frac{\xi}{\zeta}\right). \quad (\text{D4})$$

Appendix E: Degenerate points

In this appendix we present an analysis for degenerate points. A fixed point is called degenerate if all the eigenvalues of the variation matrix at the point analyzed are zero, thus rendering the centre manifold analysis impractical. The chosen method for addressing this is a change of coordinates to a polar system. Typically it is referred to as a little degenerate point if the behavior of the point becomes evident through this (or another) simple transformation. It is worth noting that this approach can be readily generalized to higher dimensions. A two-dimensional dynamical system is then considered:

$$\dot{x} = P(x, y), \quad \dot{y} = Q(x, y). \quad (\text{E1})$$

In addition, the origin is considered as a critical point to be analyzed. The change from coordinates to polar is then made:

$$r = \sqrt{x^2 + y^2}, \quad \theta = \arctan(y/x). \quad (\text{E2})$$

Therefore, the dynamical system can be expressed as follows:

$$r' = cP(rc, rs) + sQ(rc, rs), \quad (\text{E3})$$

$$\theta' = c^2 \left(\frac{Q(rc, rs)}{rc} - \frac{s}{rc^2} P(rc, rs) \right), \quad (\text{E4})$$

where, we have defined $c = \cos(\theta)$ and $s = \sin(\theta)$ for convenience.

For purposes of analyzing in the neighborhood of the origin, it is convenient to separate (x, y) into homogeneous polynomials, which in turn can be expressed as polynomials in r in polar terms, to finally stay with those of lower order:

$$P(x, y) \approx P_n(x, y) = r^n P_n(c, s), \quad (\text{E5})$$

$$Q(x, y) \approx Q_n(x, y) = r^n Q_n(c, s), \quad (\text{E6})$$

where n is the smallest order between P and Q , and at least one of them not null. The objective is then to search for directions that locally behave as an invariant local manifold or, equivalently, to find a curve that reaches or departs from 0 with a slope of $\tan \theta_0$, where θ_0 is the value that cancels θ' . This idea is encapsulated in the following theorem: [73]

“Suppose $\theta' = 0$ have $q \neq 0$ real zeros $\theta_1, \dots, \theta_q$ close to the origin in $]-\pi/2, \pi/2]$. If all of them are simple or if, for those θ_i that are multiple, the term that accompanies the smallest order of r' is non-zero, there exists for each $i = 1, \dots, q$ at least one manifold that goes to 0 with a slope of $\tan \theta_i$. The local flux over each of them is determined by the sign of the term that accompanies the lowest order of r' if it is non-zero or can be specified by calculating some term of the development of the manifold if it is zero. On the contrary, these flows and the sign of θ' in $[0, 2\pi]$ determine the local structure of the lowest-order term of θ'' .

Having said this, to determine the above-mentioned manifold, we use approximations for small r . Consequently,

$$\theta' \approx r^{n-1} (cQ_n(c, s) - sP_n(c, s)) \quad (\text{E7})$$

for some θ_0 . It then becomes necessary to evaluate the sign of the following expression (note that $\theta_0 + \pi$ is also a solution and should be evaluated if necessary):

$$r' \approx r^n (cP_n(c, s) + sQ_n(c, s)). \quad (\text{E8})$$

The sign of this expression, whether positive or negative, indicates whether the flow is repulsive or attractive in this direction. If the analysis proves to be inconclusive using this method, a graphical analysis will be carried out, as other types of analysis are beyond the intended scope of this paper.

Appendix F: Flat cosmological models

In this appendix we present the results obtained by considering the flat case for the various models presented in section V.

Dataset	$\Omega_{\phi,0}$	α	δ	H_0	\mathcal{M}	χ^2_{\min}	χ^2_{red}	AIC	BIC	ΔAIC	ΔBIC
Λ CDM											
OHD	$0.741^{+0.016}_{-0.017}$	—	—	70.69 ± 1.13	—	27.5	0.56	31.5	35.4	-1.0	-2.9
PaSNe	$0.706^{+0.019}_{-0.020}$	—	—	$73.20^{+4.99}_{-5.00}$	23.81 ± 0.01	1027.4	0.98	1033.4	1048.3	-1.8	-6.7
PaSNe+OHD	$0.726^{+0.013}_{-0.014}$	—	—	$69.78^{+0.95}_{-0.94}$	23.80 ± 0.01	1056.6	0.96	1064.6	1084.6	1.6	1.6
EP											
OHD	0.717 ± 0.046	$8.64^{+15.23}_{-15.30}$	—	$70.24^{+1.38}_{-1.34}$	—	26.9	0.56	32.9	38.7	0.4	0.4
PaSNe	$0.720^{+0.033}_{-0.037}$	$-13.48^{+26.18}_{-22.49}$	—	$73.39^{+4.97}_{-4.88}$	23.81 ± 0.01	1027.4	0.98	1035.4	1055.2	0.2	0.2
PaSNe+OHD	$0.692^{+0.031}_{-0.030}$	$14.82^{+11.95}_{-12.57}$	—	69.44 ± 0.96	23.81 ± 0.01	1054.8	0.96	1062.8	1082.8	-0.2	-0.2
EPf											
OHD	$0.739^{+0.016}_{-0.017}$	—	—	$70.68^{+1.11}_{-1.15}$	—	27.4	0.56	31.4	35.3	-1.1	-3.0
PaSNe	$0.705^{+0.019}_{-0.020}$	—	—	$73.23^{+4.96}_{-4.98}$	23.81 ± 0.01	1027.4	0.98	1033.4	1048.3	-1.8	-6.7
PaSNe+OHD	$0.724^{+0.013}_{-0.014}$	—	—	$69.79^{+0.91}_{-0.95}$	23.80 ± 0.01	1056.3	0.96	1062.3	1077.3	-0.7	-5.7
IQP											
OHD	$0.734^{+0.031}_{-0.025}$	—	$-267.6^{+816.0}_{-514.1}$	$70.52^{+1.35}_{-1.28}$	—	27.0	0.56	33.0	38.8	0.5	0.5
PaSNe	$0.732^{+0.032}_{-0.029}$	—	$3765.2^{+4633.7}_{-3047.7}$	$73.85^{+4.98}_{-4.91}$	23.80 ± 0.01	1027.8	0.98	1035.8	1055.6	0.6	0.6
PaSNe+OHD	$0.713^{+0.017}_{-0.016}$	—	$-575.3^{+517.0}_{-301.6}$	$69.56^{+0.97}_{-0.95}$	23.80 ± 0.01	1054.5	0.96	1062.5	1082.5	-0.5	-0.5
IQPf											
OHD	$0.742^{+0.016}_{-0.017}$	—	—	$70.72^{+1.12}_{-1.13}$	—	27.5	0.56	31.5	35.4	-1.0	-2.9
PaSNe	$0.706^{+0.019}_{-0.020}$	—	—	$73.24^{+4.99}_{-4.96}$	23.81 ± 0.01	1027.4	0.98	1033.4	1048.3	-1.8	-6.7
PaSNe+OHD	$0.726^{+0.013}_{-0.014}$	—	—	69.78 ± 0.93	23.80 ± 0.01	1056.6	0.96	1062.6	1077.6	-0.4	-5.4

TABLE VII: Parameters and uncertainties obtained for the cosmological models investigated assuming a spatial flat universe. The identification names and field potentials for the Λ CDM model and mimetic gravity models (EP, EPf, IQP and IQPf) are listed in Table V. The properties of these cosmological models (with $\Omega_{k,0} = 0$) are also obtained using three data sets: the Observational Hubble database from the cosmic chronometers (OHD), the Pantheon database from Type Ia supernovae (PaSNe) and the simultaneous analysis of the OHD and PaSNe data sets (OHD+PaSNe). The statistical parameters ΔAIC and ΔBIC are computed with respect to the non-flat cosmological models (presented in Table VI).

-
- [1] A. G. Riess et al. (Supernova Search Team), *Astron. J.* **116**, 1009 (1998), astro-ph/9805201.
[2] S. Perlmutter et al. (Supernova Cosmology Project), *Astrophys. J.* **517**, 565 (1999), astro-ph/9812133.
[3] D. N. Spergel et al. (WMAP), *Astrophys. J. Suppl.* **148**, 175 (2003), astro-ph/0302209.
[4] P. A. R. Ade et al. (Planck), *Astron. Astrophys.* **571**, A16 (2014), 1303.5076.
[5] D. J. Eisenstein et al. (SDSS), *Astrophys. J.* **633**, 560 (2005), astro-ph/0501171.
[6] T. P. Sotiriou and V. Faraoni, *Rev. Mod. Phys.* **82**, 451 (2010), 0805.1726.
[7] A. A. Starobinsky, *Phys. Lett. B* **91**, 99 (1980).
[8] S. Nojiri, S. D. Odintsov, and V. K. Oikonomou, *Phys. Rept.* **692**, 1 (2017), 1705.11098.
[9] S. Nojiri and S. D. Odintsov, *J. Phys. Conf. Ser.* **66**, 012005 (2007), hep-th/0611071.
[10] A. H. Chamseddine and V. Mukhanov, *JHEP* **11**, 135 (2013), 1308.5410.
[11] E. A. Lim, I. Sawicki, and A. Vikman, *JCAP* **05**, 012 (2010), 1003.5751.
[12] P. Jiroušek, K. Shimada, A. Vikman, and M. Yamaguchi (2022), 2212.14867.
[13] L. Sebastiani, S. Vagnozzi, and R. Myrzakulov, *Adv. High Energy Phys.* **2017**, 3156915 (2017), 1612.08661.
[14] A. H. Chamseddine, V. Mukhanov, and A. Vikman, *JCAP* **06**, 017 (2014), 1403.3961.
[15] S. Nojiri and S. D. Odintsov (2014), [Erratum: *Mod.Phys.Lett.A* 29, 1450211 (2014)], 1408.3561.
[16] R. Myrzakulov, L. Sebastiani, and S. Vagnozzi, *Eur. Phys. J. C* **75**, 444 (2015), 1504.07984.
[17] A. V. Astashenok, S. D. Odintsov, and V. K. Oikonomou, *Class. Quant. Grav.* **32**, 185007 (2015), 1504.04861.
[18] S. Nojiri, S. D. Odintsov, and V. K. Oikonomou, *Phys. Rev. D* **94**, 104050 (2016), 1608.07806.
[19] S. Nojiri, S. D. Odintsov, and V. K. Oikonomou, *Phys. Lett. B* **775**, 44 (2017), 1710.07838.
[20] A. Z. Kaczmarek and D. Szczekśniak, *Sci. Rep.* **11**, 18363 (2021), 2105.05050.
[21] G. Cognola, R. Myrzakulov, L. Sebastiani, S. Vagnozzi, and S. Zerbini, *Class. Quant. Grav.* **33**, 225014 (2016), 1601.00102.
[22] A. Casalino, M. Rinaldi, L. Sebastiani, and S. Vagnozzi, *Class. Quant. Grav.* **36**, 017001 (2019), 1811.06830.
[23] A. Casalino, M. Rinaldi, L. Sebastiani, and S. Vagnozzi, *Phys. Dark Univ.* **22**, 108 (2018), 1803.02620.
[24] S. Tsujikawa, *Class. Quant. Grav.* **30**, 214003 (2013), 1304.1961.
[25] V. Faraoni, *Cosmology in scalar tensor gravity* (2004), ISBN 978-1-4020-1988-3.

- [26] T. Kobayashi, Rept. Prog. Phys. **82**, 086901 (2019), 1901.07183.
- [27] S. Capozziello, F. Occhionero, and L. Amendola, Int. J. Mod. Phys. D **1**, 615 (1993).
- [28] S. D. Odintsov and V. K. Oikonomou, Phys. Rev. D **96**, 104049 (2017), 1711.02230.
- [29] E. J. Copeland, A. R. Liddle, and D. Wands, Phys. Rev. D **57**, 4686 (1998), gr-qc/9711068.
- [30] N. Roy and N. Banerjee, Eur. Phys. J. Plus **129**, 162 (2014), 1402.6821.
- [31] J.-g. Hao and X.-z. Li, Phys. Rev. D **67**, 107303 (2003), gr-qc/0302100.
- [32] S. D. Odintsov and V. K. Oikonomou, Phys. Rev. D **93**, 023517 (2016), 1511.04559.
- [33] J. Dutta, W. Khylllep, E. N. Saridakis, N. Tamanini, and S. Vagnozzi, JCAP **02**, 041 (2018), 1711.07290.
- [34] G. Leon and E. N. Saridakis, JCAP **04**, 031 (2015), 1501.00488.
- [35] O. Hrycyna and M. Szydlowski, Phys. Rev. D **88**, 064018 (2013), 1304.3300.
- [36] C. G. Boehmer, E. Jensko, and R. Lazkoz, Eur. Phys. J. C **82**, 500 (2022), 2201.09588.
- [37] S. Carloni and J. P. Mimoso, Eur. Phys. J. C **77**, 547 (2017), 1701.00231.
- [38] M. Goliath and G. F. R. Ellis, Phys. Rev. D **60**, 023502 (1999), gr-qc/9811068.
- [39] A. O. Yilmaz and E. Güdekli, Sci. Rep. **11**, 2750 (2021).
- [40] C. G. Boehmer and N. Chan (2014), 1409.5585.
- [41] S. Bahamonde, C. G. Böhmmer, S. Carloni, E. J. Copeland, W. Fang, and N. Tamanini, Phys. Rept. **775-777**, 1 (2018), 1712.03107.
- [42] E. Di Valentino, A. Melchiorri, and J. Silk, Nature Astron. **4**, 196 (2019), 1911.02087.
- [43] W. Handley, Phys. Rev. D **103**, L041301 (2021), 1908.09139.
- [44] E. Di Valentino, A. Melchiorri, and J. Silk, Astrophys. J. Lett. **908**, L9 (2021), 2003.04935.
- [45] G. Leon, J. Saavedra, and E. N. Saridakis, Classical and Quantum Gravity **30**, 135001 (2013).
- [46] C. R. Fadrakas, G. Leon, and E. N. Saridakis, Classical and Quantum Gravity **31**, 075018 (2014).
- [47] J. Magana, M. H. Amante, M. A. Garcia-Aspeitia, and V. Motta, Mon. Not. Roy. Astron. Soc. **476**, 1036 (2018), 1706.09848.
- [48] D. M. Scolnic et al. (Pan-STARRS1), Astrophys. J. **859**, 101 (2018), 1710.00845.
- [49] D. Foreman-Mackey, D. W. Hogg, D. Lang, and J. Goodman, Publ. Astron. Soc. Pac. **125**, 306 (2013), 1202.3665.
- [50] M. Moresco et al., Living Rev. Rel. **25**, 6 (2022), 2201.07241.
- [51] R. Jimenez and A. Loeb, Astrophys. J. **573**, 37 (2002), astro-ph/0106145.
- [52] C. Corral, N. Cruz, and E. González, Phys. Rev. D **102**, 023508 (2020), 2005.06052.
- [53] A. Conley et al. (SNLS), Astrophys. J. Suppl. **192**, 1 (2011), 1104.1443.
- [54] H.-K. Deng and H. Wei, Eur. Phys. J. C **78**, 755 (2018), 1806.02773.
- [55] K. Asvesta, L. Kazantzidis, L. Perivolaropoulos, and C. G. Tsagas, Mon. Not. Roy. Astron. Soc. **513**, 2394 (2022), 2202.00962.
- [56] S. Cao, J. Ryan, and B. Ratra, Mon. Not. Roy. Astron. Soc. **504**, 300 (2021), 2101.08817.
- [57] R. Kessler and D. Scolnic, Astrophys. J. **836**, 56 (2017), 1610.04677.
- [58] H. Akaike, IEEE Transactions on Automatic Control **19**, 716 (1974).
- [59] G. Schwarz, Annals Statist. **6**, 461 (1978).
- [60] W. Yang, W. Giarè, S. Pan, E. Di Valentino, A. Melchiorri, and J. Silk, Phys. Rev. D **107**, 063509 (2023), 2210.09865.
- [61] S. Vagnozzi, A. Loeb, and M. Moresco, Astrophys. J. **908**, 84 (2021), 2011.11645.
- [62] S. Vagnozzi, E. Di Valentino, S. Gariazzo, A. Melchiorri, O. Mena, and J. Silk, Phys. Dark Univ. **33**, 100851 (2021), 2010.02230.
- [63] S. Dhawan, J. Alsing, and S. Vagnozzi, Mon. Not. Roy. Astron. Soc. **506**, L1 (2021), 2104.02485.
- [64] E. Abdalla et al., JHEAp **34**, 49 (2022), 2203.06142.
- [65] N. Aghanim et al. (Planck), Astron. Astrophys. **641**, A6 (2020), [Erratum: Astron. Astrophys. 652, C4 (2021)], 1807.06209.
- [66] E. Rosenberg, S. Gratton, and G. Efsthathiou, Mon. Not. Roy. Astron. Soc. **517**, 4620 (2022), 2205.10869.
- [67] M. Tristram et al. (2023), 2309.10034.
- [68] D. Brout et al., Astrophys. J. **938**, 110 (2022), 2202.04077.
- [69] A. G. Riess, S. Casertano, W. Yuan, J. B. Bowers, L. Macri, J. C. Zinn, and D. Scolnic, Astrophys. J. Lett. **908**, L6 (2021), 2012.08534.
- [70] A. G. Riess et al., Astrophys. J. Lett. **934**, L7 (2022), 2112.04510.
- [71] A. G. Riess, S. Casertano, W. Yuan, L. M. Macri, and D. Scolnic, The Astrophysical Journal **876**, 85 (2019).
- [72] M. Petronikolou, S. Basilakos, and E. N. Saridakis, Phys. Rev. D **106**, 124051 (2022), 2110.01338.
- [73] J. I. Aranda Iriarte, in *XV Congreso de ecuaciones diferenciales y aplicaciones, V Congreso de Matemática Aplicada : Vigo, 23-26 septiembre 1997* (Servizo de Publicacions, 1998), vol. 1, pp. 157–162, ISBN 84-8158-093-7.